GEOMAGNETIC VARIATIONS IN THE NORTHWEST ATLANTIC: IMPLICATIONS FOR THE ELECTRICAL RESISTIVITY OF THE OCEANIC LITHOSPHERE

by

KENNETH ALLEN POEHLS

B.S. University of California at Los Angeles
(1971)

SUBMITTED IN PARTIAL FULFILLMENT OF THE REQUIREMENTS FOR THE DEGREE OF DOCTOR OF PHILOSOPHY

at the

MASSACHUSETTS INSTITUTE OF TECHNOLOGY

and the

WOODS HOLE OCEANOGRAPHIC INSTITUTION

October, 1975

Signature of Author....Kenneth A. Poehls.....
Joint Program in Oceanography, Massachusetts Institute of Technology - Woods Hole Oceanographic Institution, and Department of Earth and Planetary Sciences, Massachusetts Institute of Technology, October 1975

Certified by .....R. P. Von Herzen.....
Thesis Supervisor

Accepted by .....M. Edmond.....
Chairman, Joint Oceanography Committee in the Earth Sciences, Massachusetts Institute of Technology - Woods Hole Oceanographic Institution

GEOMAGNETIC VARIATIONS IN THE NORTHWEST ATLANTIC: IMPLICATIONS FOR THE ELECTRICAL RESISTIVITY OF THE OCEANIC LITHOSPHERE

by

Kenneth Allen Poehls

Submitted to the Massachusetts Institute of Technology-Woods Hole Oceanographic Institution Joint Program in Oceanography on October 23, 1975, in partial fulfillment of the requirements for the degree of Doctor of Philosophy.

ABSTRACT

A geomagnetic variation study on mature oceanic lithosphere in the North Atlantic just south of Bermuda has revealed the presence of at least one layer of low electrical resistivity. The low resistivity layer of approximately 10 ohm-m has been found at three widely spaced seafloor sites with crustal ages of 85, 110 and 150 million years. There is also evidence that the resistivity increases to greater than 20 ohm-m below about 100 km.

Apparent resistivity and phase versus period are calculated using the vertical gradient of the horizontal magnetic field variations to estimate the seafloor electric field. The vertical gradient method assumes that the seasurface magnetic variations can be estimated from a nearby land station and that no local magnetic induction occurs at either reference or seafloor site. Both assumptions are critically evaluated during the analysis.

Seafloor observations are modeled using the Monte Carlo technique. Estimates of the smoothed resistivity structure as well as the resolution and precision of the estimates are made using the Backus-Gilbert method. Models are shown to be severely data limited. Resolution is found to be poor in the upper 30-40 km of the lithosphere due to the lack of reliable data at periods shorter than 30 minutes. The uncertainty involved in estimating the magnetic field at the seasurface

and the large error estimates combine to give low overall precision. The diurnal results do not agree with the continuum results if the continuum is corrected for latitudinal variations of the source field between the reference station and seafloor sites.

Data at periods as short as 10 minutes are required to resolve structures in the upper 30 km of the mantle. Artificial source fields may be necessary to obtain periods short enough to resolve crustal features. Periods longer than diurnal will be required to study sub-lithospheric resistivity variations.

Thesis Supervisor: Dr. Richard P. Von Herzen

Title: Senior Scientist

ACKNOWLEDGEMENTS

My special thanks go to Dr. Richard Von Herzen who allowed me to collaborate with him on the seafloor magnetometer program. The data in this thesis could not have been collected without his support, assistance and guidance. Drs. Richard Von Herzen, John Hermance, Theodore Madden, and John Sclater have provided assistance and encouragement on many occasions.

Dr. D.I. Gough kindly provided unpublished magnetograms from Bermuda that were used in this study. Dr. Roy Hyndman loaned us a land magnetometer to be used as a reference station on Bermuda in 1974. The Bermuda Biological Station tended the magnetometer for us. Drs. C.S. Cox and J.H. Filloux kindly provided the unpublished seafloor electric field data shown in Figure 4.5.

We are indebted to the MODE Project and to Jess Stanbrough for the ship time required to deploy and recover our instruments. Many people associated with these cruises willingly assisted in the deployment and recovery operations.

My appreciation must also be extended to Paul Murray, Ray Davis and Richard Zuck for their part in the design, construction, and preparation of the seafloor instruments for deployment.

Most of this work was supported through the National Science Foundation Grants GA 42651 and DES74-12730, Office of Naval Research Contracts N00014-66-C-0241; NR 083-004 and N00014-77-C-0262; NR 083-004, and the Education Office of the Woods Hole Oceanographic Institution.

TABLE OF CONTENTS

LIST OF FIGURES

LIST OF TABLES

COMMONLY USED SYMBOLS AND ABBREVIATIONS

A	Transfer function, usually with subscripts
$C_{ij}(f)$	Auto- or cross-spectrum depending on subscript
cpd	Cycles per day
d	Depth of the seawater layer
$\vec{E}, E_i$	Electric field
f	Frequency
$\vec{H}, H_i$	Magnetic field
i	$\sqrt{-1}$
M_2	Lunar semi-diurnal harmonic
R	Ratio of seafloor to seasurface magnetic variations
S_1, S_2, S_3	Solar diurnal harmonics
X, Y	Magnetic coordinates in geographic north and east directions respectively. May have subscripts designating a particular station
x, y	Magnetic coordinates as above representing seafloor variations. If used as a subscript they designate geographic north and east respectively
z	Vertical direction or depth
$Z(\omega)$	Complex impedance
ρ	Electrical resistivity
ρ_a	Apparent resistivity
ω	Angular frequency

σ	Electrical conductivity
σ_1	Electrical conductivity of seawater
ϕ	Transfer function phase angle
ψ	Impedance phase angle
μ_o	Magnetic permeability of free space
ν	Degrees of freedom
*	Complex conjugate
$\langle\ \rangle$	Expected value

CHAPTER I

INTRODUCTION

1.1 BACKGROUND

During the past two decades the use of electromagnetic and magnetic methods to study the electrical conductivity of the earth has become a respected geophysical tool. The early single station methods of Cagniard (1953) and Tikhonov (1950) have been expanded into large array methods surveying thousands of square miles (Gough, 1973; Bennett and Lilley, 1973a, b; Porath et al., 1970; Caner et al., 1967; Camfield et al., 1971). Most of the work, however, has been confined to land areas.

More recently it became obvious that oceanic areas have a significantly different conductivity structure (Fig. 1.1). Geomagnetic measurements on the landward side of coasts (Parkinson, 1964; Schmucker, 1970; Hyndman and Cochrane, 1971; Srivastava and White, 1971) showed large concentrations of electrical currents offshore in most places. It was still not known whether the currents were in the seawater or oceanic upper mantle.

In 1967 Filloux conducted the first electromagnetic sounding on the seafloor to study the origins of the coast

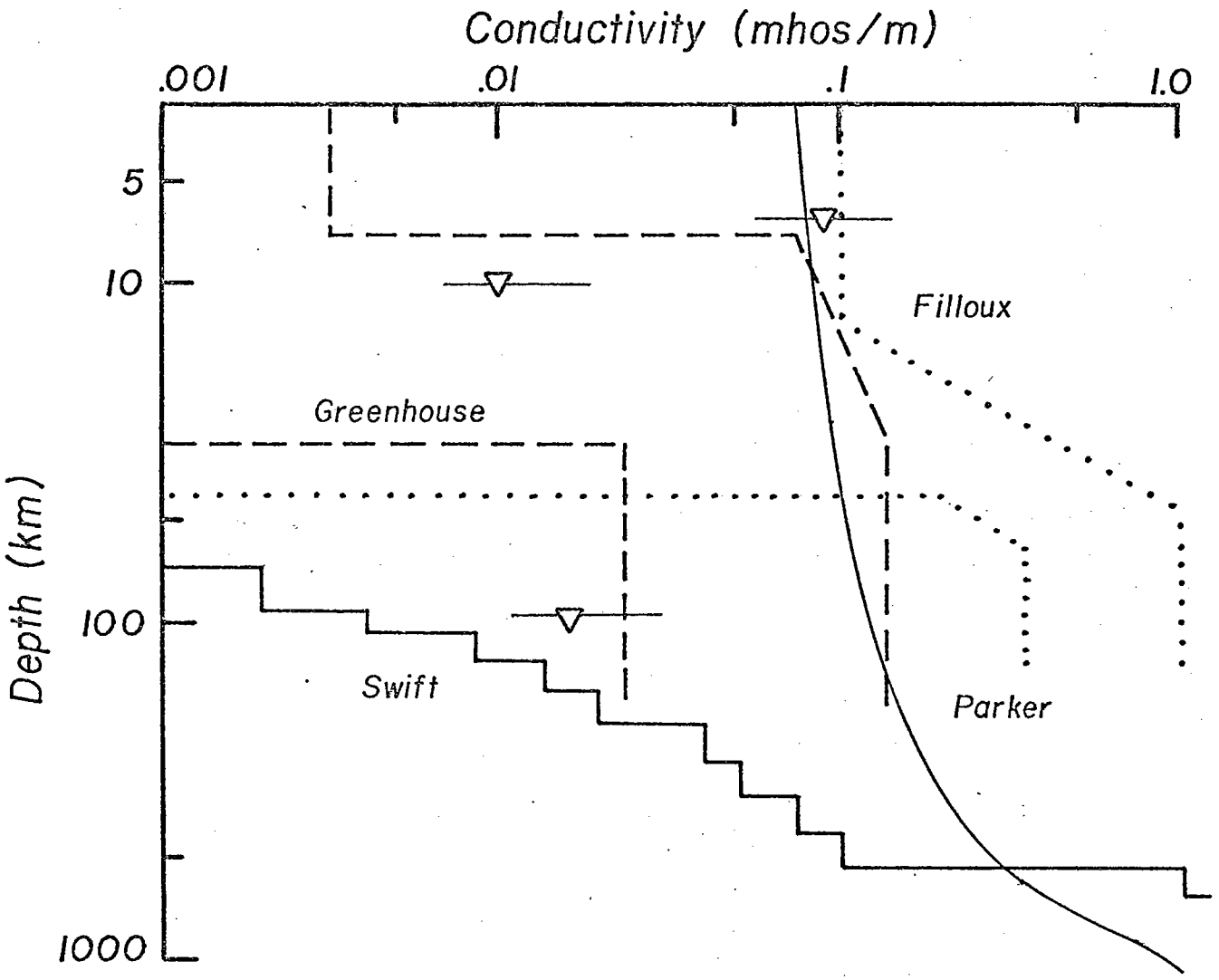

Figure 1.1 Some proposed conductivity structures for the outer 1000 km of the earth. Oceanic structures of Filloux (dotted lines) and Greenhouse (dashed lines); global spherical harmonic analysis by Parker (thin solid line); Icelandic structure by Hermance (triangles); continental structure by Swift (heavy solid line).

effect. The results (Filloux, 1967; Cox et al., 1970) showed that most of the electric currents flowed in the highly conductive (0.2-1.0 mho/m at 40 km) upper mantle. Virtually the same experiment was repeated by Greenhouse (1972) using three-component magnetometers. His results indicate a less conductive oceanic mantle (about 0.03-0.1 mho/m at 40 km) and more electrical currents flowing in the seawater. These two studies clearly indicated the conductivity contrasts that might exist between oceanic and continental regions.

Electromagnetic soundings on islands further substantiate the presence of an increased conductivity at depth (Hermance and Grillot, 1970; Hermance and Garland, 1968; Larsen, 1975). However, it is not known how much the structure is dominated by the anomalous nature of the island itself.

Global spherical harmonic analyses have generated more conflicting results. Parker (1970) finds a conductivity of 0.1 mho/m in the upper 100 km of the earth. Jady (1974) used the first three diurnal harmonics to show the conductivity was substantially lower at about 0.02-0.05 mho/m. Spherical analyses have very poor resolution in the upper

100-200 km because of the uniformity requirements on both structure and source field. Thus, it is hard to judge how these results apply to any specific region.

On land an electromagnetic survey is employed largely to study the thermal structure of a particular region. The electrical conductivity of most semiconducting materials increases exponentially with temperature (Grant and West, 1965; Parkhomenko, 1967) so regionally changing conductivities may be indicative of changing temperatures. If the temperature gets high enough the material begins to melt; melting is accompanied by order of magnitude increases in electrical conductivity (Presnall et al., 1972; Watt, 1974). However, an interpretation based on temperature variations alone is not always correct because conductivity may also dramatically change with mineralogy, composition, phase, or water content.

The plate tectonic models of oceanic thermal evolution and structure are all very simple away from the ridge crest (McKenzie, 1967; Sclater and Francheteau, 1970; Parker and Oldenburg, 1973). Basically, the lithosphere cools as it moves away from the ridge crest and ages. Whether or not it ever reaches equilibrium is still disputed (Parker and Oldenburg, 1973; Sclater et al., 1975). Whatever happens, however, the temperature monotonically increases with depth.

Material below the lithosphere is believed to be convecting (McKenzie, 1969; Turcotte and Oxburgh, 1972; Richter, 1973). The thickness of this convecting region is believed to be about 500-600 km (McKenzie et al., 1974; Richter, 1973). This estimate is based largely upon the fact that earthquakes are observed only at depths shallower than 650 km (Isacks and Molnar, 1971). The thermal gradient within a convecting system should be close to adiabatic (Richter, 1973). An adiabatic gradient would cause little, if any, change in the electrical conductivity of mantle materials.

The simple thermally controlled electrical resistivity structure implied by this discussion (see Model A, Fig. 5.2) would differ little from the continental structure and certainly could not produce the observed coast effect. Several inferences might be drawn from these observations. 1) The seafloor off California where Filloux and Greenhouse performed their studies is anomalous seafloor, possibly due to the active tectonic setting. 2) The electrical structure of the seafloor is not dominated by the thermal structure but is controlled, at least in the lithosphere, by changing composition, mineralogy, phase, or water content. In either case, the electrical conductivity supplies information about the lithosphere not available through other techniques.

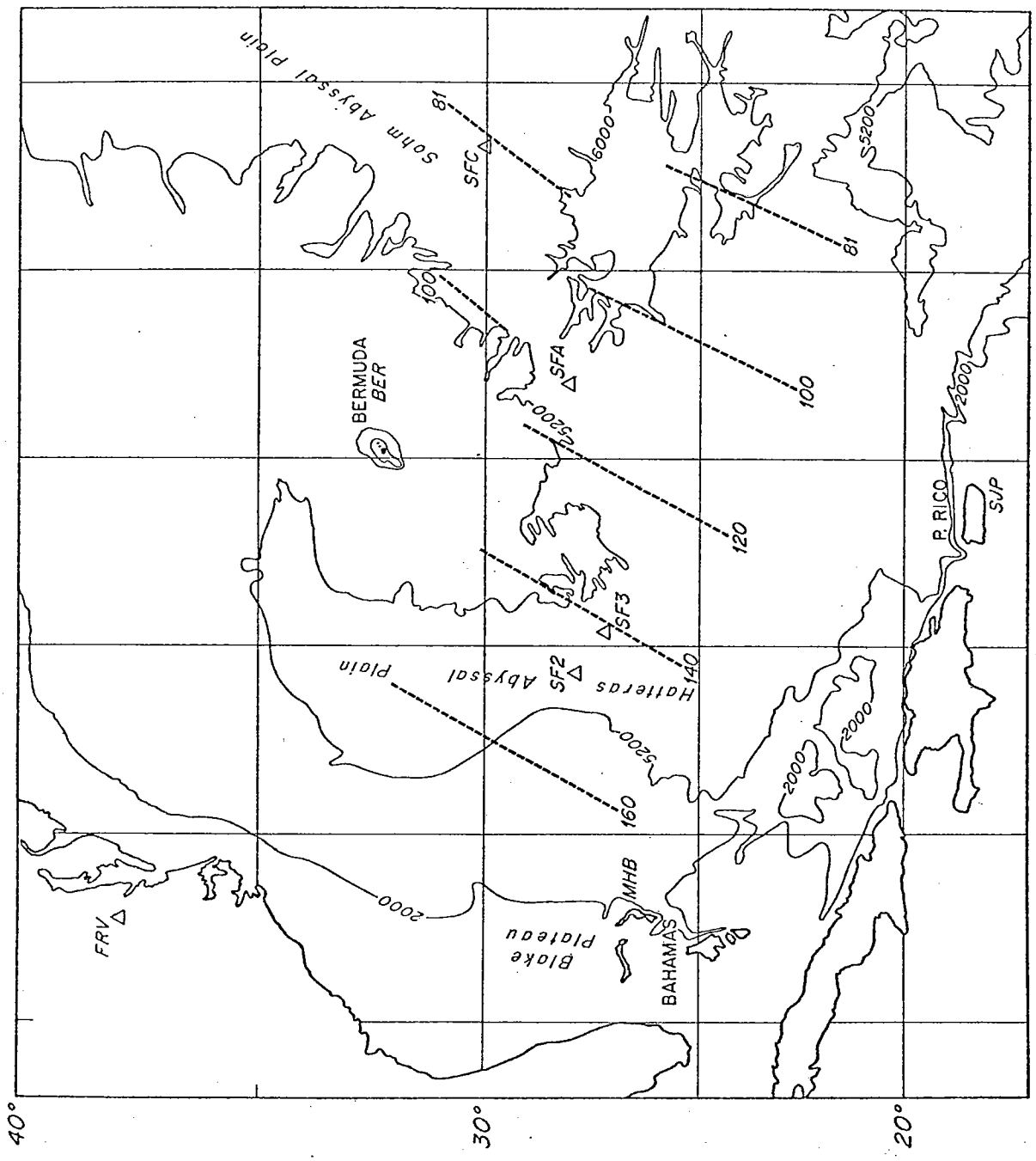

Figure 1.2 Location map for the study area and magnetometer sites. Bathymetric contours are in meters. Dashed lines are isochrons.

1.2 EXPERIMENTAL SETTING

Previous investigators have dealt with the electrical structure of the ocean basins only as an ancillary extension to the coastal problem. The purpose of the present work is to eliminate the perturbing effects of the continental margin and to study the resistivity structure of an ocean basin. The geographical location of the experiment is the seafloor approximately 3-5° south of Bermuda (Fig. 1.2). This area is attractive because of its apparent geological simplicity and old age.

As can be seen from the map, Sites SF2, SF3 (hereafter referred to collectively as SF) and SFC are located on the Hatteras and Sohm Abyssal plains respectively. The Hatteras Abyssal Plain sites are characterized by flat-lying sediments usually less than a half kilometer thick (Ewing et al., 1974) with occasional basement outcrops of 10-20 m relief. Site SF3 is nearer the eastern edge of the plain and has more outcropping basement (Bush, 1975). SFC is located on the southern extremity of the Sohm Abyssal Plain. Basement outcrops in the form of northeast-southwest striking ridges with several hundred meters of relief are visible 20 miles south of the site but become less frequent in the instrument area. Again, there is usually less than a half kilometer of flat-lying sediments except in some isolated ponds.

TABLE 1.1

Seafloor and Reference Stations Used in this Analysis

Station	Position	Recording Time	Comments
SF2	27°50.6'N 70°40.2'W	7303240000 - 7305060000 Z	water depth is 5390 m
SF3	27°08.8'N 69°31.8'W	7306170030 - 7306300030 Z	water depth is 5390 m
SFA	28°01.1'N 63°00.1'W	7407301900 - 7410221900 Z	water depth is 5480 m
SFC	30°00.2'N 56°30.6'W	7408032300 - 7410262300 Z	water depth is 5540 m
BER	32°23' N 64°41' W	7303030000 - 7306242300 Z	hourly means only
		7408070000 - 7410180900 Z	hourly means only
MHB	26°30 N 77°20' W	7303110000 - 7306282300 Z	hourly means only
FRV	39°30' N 77°30' W	continuous	observatory
SJP	18°28' N 66°07' W	continuous	observatory

The location of SFA is in the abyssal hills southwest of the Sohm Abyssal Plain. The region might be characterized by long ridges sometimes 0.5-1 km high striking north-northeast at 10-20 km intervals. Large sediment ponds are found between most ridges.

All sites sample old and presumably stable seafloor. However, a 10 m.y. offset of the isochrons is found between SFA and SFC (Pitman and Talwani, 1972). SFA is located very near, if not in, the Kane Fracture Zone and might be considered anomalous.

Other magnetometer stations that will be used are listed in Table 1.1. FRV is the geomagnetic observatory at Fredericksburg, Virginia. BER, SJP, and MHB are three island stations at St. George, Bermuda, San Juan, Puerto Rico, and Marsh Harbor, Bahamas.

1.3 GEOMAGNETIC VARIATIONS: VERTICAL GRADIENT OF THE HORIZONTAL FIELD

Electromagnetic sounding methods are all derived from the fact that an external time-varying magnetic field will induce an electric current within a conducting body (Landau and Lifshitz, 1960). How well this electric current flows through the conductor or alternatively how rapidly the current

dissipates energy is dependent upon the physical properties of the conductor. What can be measured at the earth's surface is the induced electric field and/or the total (both external and induced) magnetic field.

The magnetotelluric method (Cagniard, 1953) is by far the easiest method of obtaining an estimate of the subsurface conductivity from the surface measurements. Cagniard showed that the ratio of orthogonal electric and magnetic field components is easily related to an apparent resistivity of the earth at every frequency. The apparent resistivity is a measure of the average resistivity within the region the frequency samples. The Cagniard method assumes a uniform source field and an isotropic, layered, conductivity structure. Improvements and modifications were later made to include non-uniform source fields (Price, 1962; Srivastava, 1965) and inhomogeneities (Abramovici, 1974).

Without measuring the seafloor electric field, Cagniard's method cannot be immediately utilized. However, the vertical gradient of the horizontal magnetic field variations can be related to the electric field through Maxwell's equation

$$\nabla \times \vec{H} = j = \sigma \vec{E}$$

or in components

$$\frac{\partial H_z}{\partial y} - \frac{\partial H_y}{\partial z} = \sigma E_x$$

$$\frac{\partial H_x}{\partial z} - \frac{\partial H_z}{\partial x} = \sigma E_y$$

The key assumption to the vertical gradient method is that horizontal gradients are much smaller than vertical gradients. If the structure is layered and isotropic there are only very small induced vertical fields which have horizontal wavelengths of the same length scale as the horizontal inducing fields (see Section 3.2). Vertical source fields also have similarly long horizontal wavelengths. The only significant vertical fields of short wavelength found at mid-latitudes are induced by inhomogeneities in the structure which are excluded by the assumption of lateral homogeneity. Although it is not possible to prove that the vertical fields are everywhere uniform without an array of instruments, it seems to be a good assumption as long as there are no induced vertical variations. The magnetotelluric method can now be rewritten in the frequency domain as

$$Z(\omega) = \frac{E_x}{H_y} = -\frac{\partial H_y/\partial z}{\sigma_1 H_y} = -\frac{E_y}{H_x} = -\frac{\partial H_x/\partial z}{\sigma_1 H_x} \qquad \text{Eq. 1.1}$$

where $Z(\omega)$ is the Cagnaird impedance at angular frequency ω.

The ocean is an ideal environment for the use of this method. The high conductivity of seawater (about 3 mho/m) creates a large vertical gradient, so if simultaneous magnetograms are available at the seasurface and seafloor, the method is easily applied. A significant part of this thesis deals with the difficulties of estimating the seasurface variations.

A more useful expression for $Z(\omega)$ at the seasurface is obtained from the equations governing the magnetic field within a conducting layer (Schmucker, 1970). Equation 1.1 then becomes

$$Z(\omega) = i\omega\mu_0 \frac{\cosh\sqrt{i\omega\mu_0\sigma_1}\,d - R}{\sqrt{i\omega\mu_0\sigma_1}\,\sinh\sqrt{i\omega\mu_0\sigma_1}\,d} \qquad \text{Eq. 1.2}$$

where $R=H(d)/H(0)$, μ_0 is the magnetic permeability, and d is the thickness of the conducting first layer with conductivity σ_1 (seawater in this case). This is an exact solution with no assumptions; the source field wavenumber can be easily incorporated into the expression if it becomes large. The impedance can be recalculated at the seafloor using the same equations.

Equation 1.2 is often simplified for long periods by using the thin sheet approximation (Price, 1949). If the skin depth of the particular frequency is much greater than the thickness of the layer, the electric field at the top and

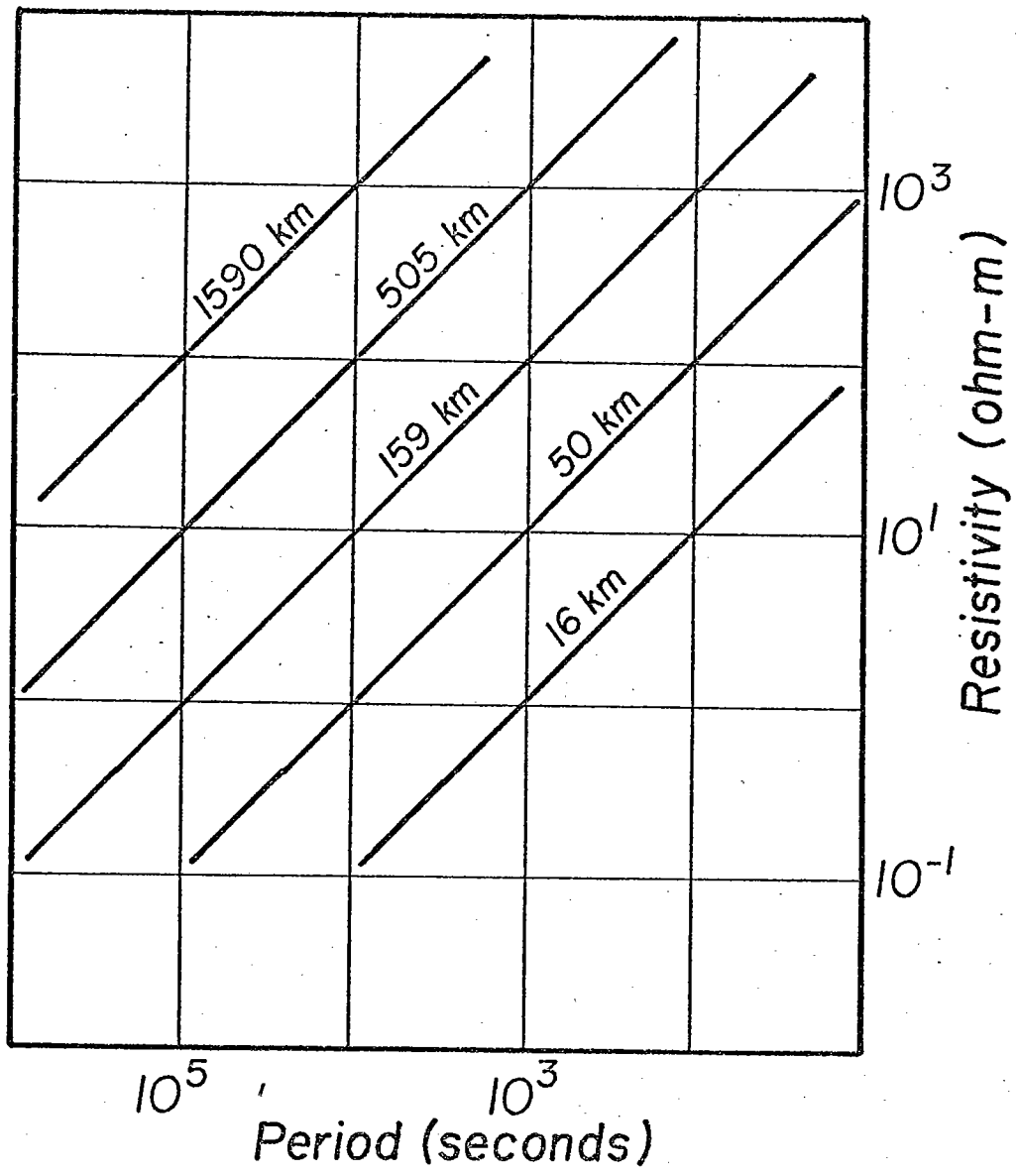

Figure 1.3 Skin depths for various combinations of period versus resistivity. The resistivity of seawater is approximately 0.3 ohm-m.

bottom of the layer approach equality. Equation 1.2 reduces to

$$Z(\omega) = \frac{R-1}{\sigma_1 d} \qquad \text{Eq. 1.3}$$

The skin depth is given by the reciprocal of the real part of $\sqrt{i\omega\mu_o\sigma}$ from Eq. 1.2. Figure 1.3 shows skin depths for various combinations of periods and conductivities. The skin depth becomes much greater than the depth of the oceans only at periods longer than diurnal.

The format for the rest of this thesis easily falls out of the preceding discussion. The important observational parameter is R, the ratio of the seafloor and seasurface magnetic fields. Chapter 2 and 3 will concern themselves with the calculation of the frequency dependent transfer functions (R) from the field data while the final two chapters (4 and 5) will interpret the transfer functions in terms of possible electrical resistivity structures and their geophysical and geological implications.

CHAPTER II

INSTRUMENTATION AND DATA COLLECTION

The accuracy of a geomagnetic analysis or any time series analysis is in the end always determined by how truly the time series samples the physical process; this in turn is some function of the instrumentation. The field work involved with this thesis requires both seafloor and land instruments.

2.1 SEAFLOOR INSTRUMENTS

The seafloor instruments (shown schematically in Figure 2.1) were designed and built at Woods Hole Oceanographic Institution by Paul Murray. The electronics are housed in a 7 1/2 inch O.D. aluminum pressure case mounted on a combination tripod support, external battery, and anchor. Three glass spheres tethered to the pressure case by a 5 m nylon line serve as floatation. The instrument can be recalled acoustically and/or an internal backup timer can be preset. In either case, the release is achieved by flooding the vacuum chamber which holds the clamshell together.

The 1973 prototype instrument differed principally in the support stand and anchor release. The stand was a large

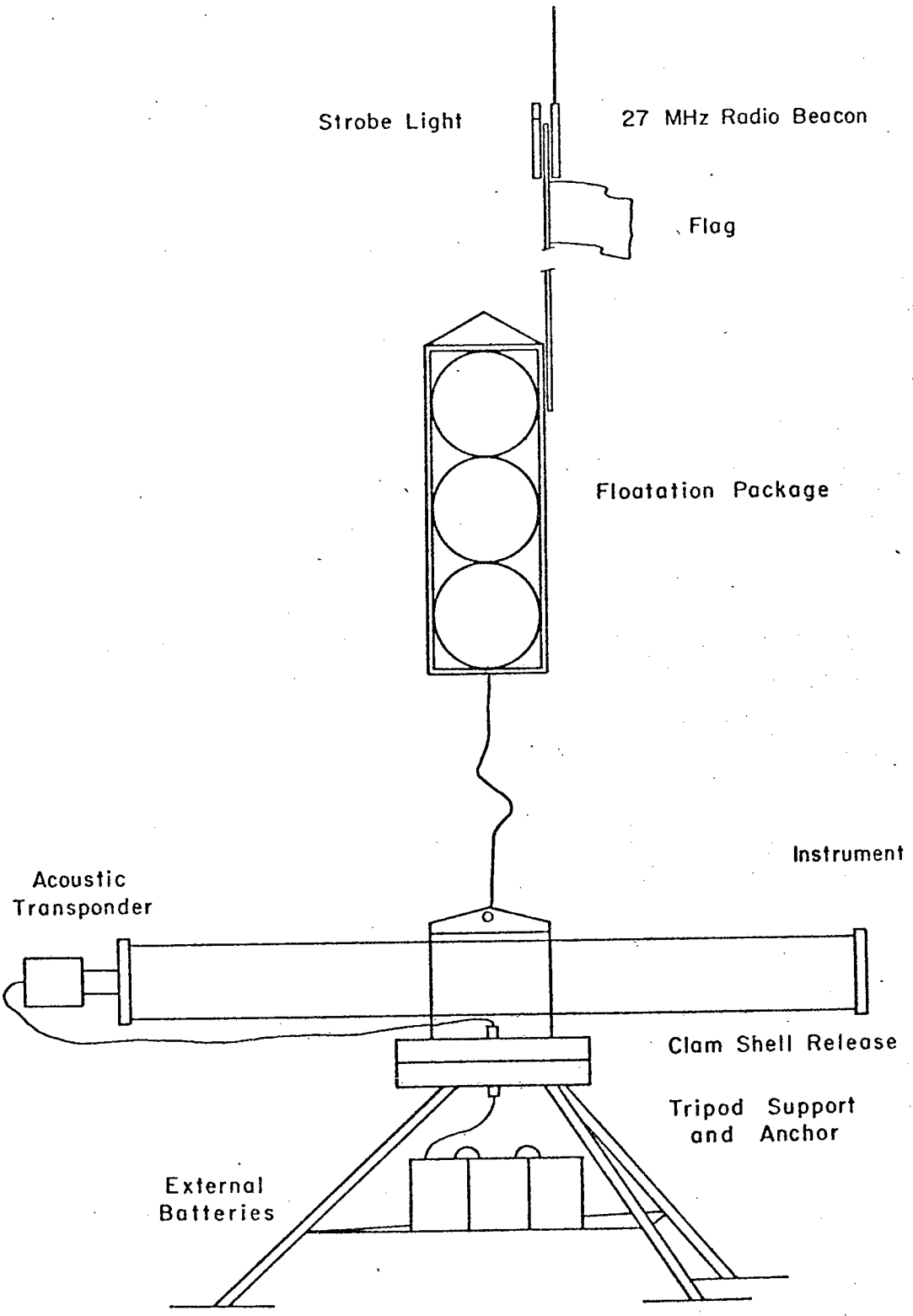

Figure 2.1 Schematic diagram of the 1974 seafloor instrumentation.

tetrahedron with floatation mechanically fastened to the top. A bolt actuated release device (AMF) was used instead of the vacuum device.

Each instrument has six thin-film inductors as sensors. Each sensor will linearly respond to magnetic field changes along its major axis. Sensor response to magnetic changes along the minor axis is negligible. Within the instrument three sets of oppositely polarized sensor pairs measure the magnetic field along three perpendicular directions. In the 1973 instruments one of the sensors was replaced by a temperature sensor. The sensors have field sensitive inductances with circuit resonant frequencies of approximately 5 mHz yielding a sensitivity of about .1 gamma. Field values are recorded digitally as the number of cycles per unit gate time (approximately 8 seconds) every 64 seconds for each sensor. The 1973 instruments recorded values for the total field in all directions. In order to obtain longer recording periods, the 1974 instruments were modified to record only the 12 least significant bits of data (0-4095) by dropping the most significant bits.

The orientation of the 1973 seafloor instrument was determined by comparing the magnitudes and signs of the total magnetic field values recorded by each sensor after

the recorded instrument tilt was removed to the geomagnetic reference field values. Uncertainties in the measured total field values of 500-1000 gammas limited the orientation accuracy to ±10°. This was improved upon in the 1974 instruments by photographically recording the attitude and direction of a compass.

The instruments are calibrated in two ways: 1) for temperature sensitivity, and 2) for magnetic field sensitivity. The temperature coefficients and field sensitivity are found to be independent. Temperature calibration consists of the measurement of the characteristic sensor frequencies for a null field at two widely separated temperatures (ambient temperature, about 25°C, and ice water, about 1°C). Temperature coefficients are all in the range of several hundred gammas per degree centigrade. Although the results are reproducible it is difficult to tell how accurate they are. The sensors are housed in an evacuated brass cannister which is not necessarily at the same temperature as its surroundings during the measurements.

Magnetic field calibration was accomplished using a set of calibrated Helmholtz coils. Sensors are placed in the center of the coils for calibration from plus to minus the earth's main field. Calibration curves for the 1973

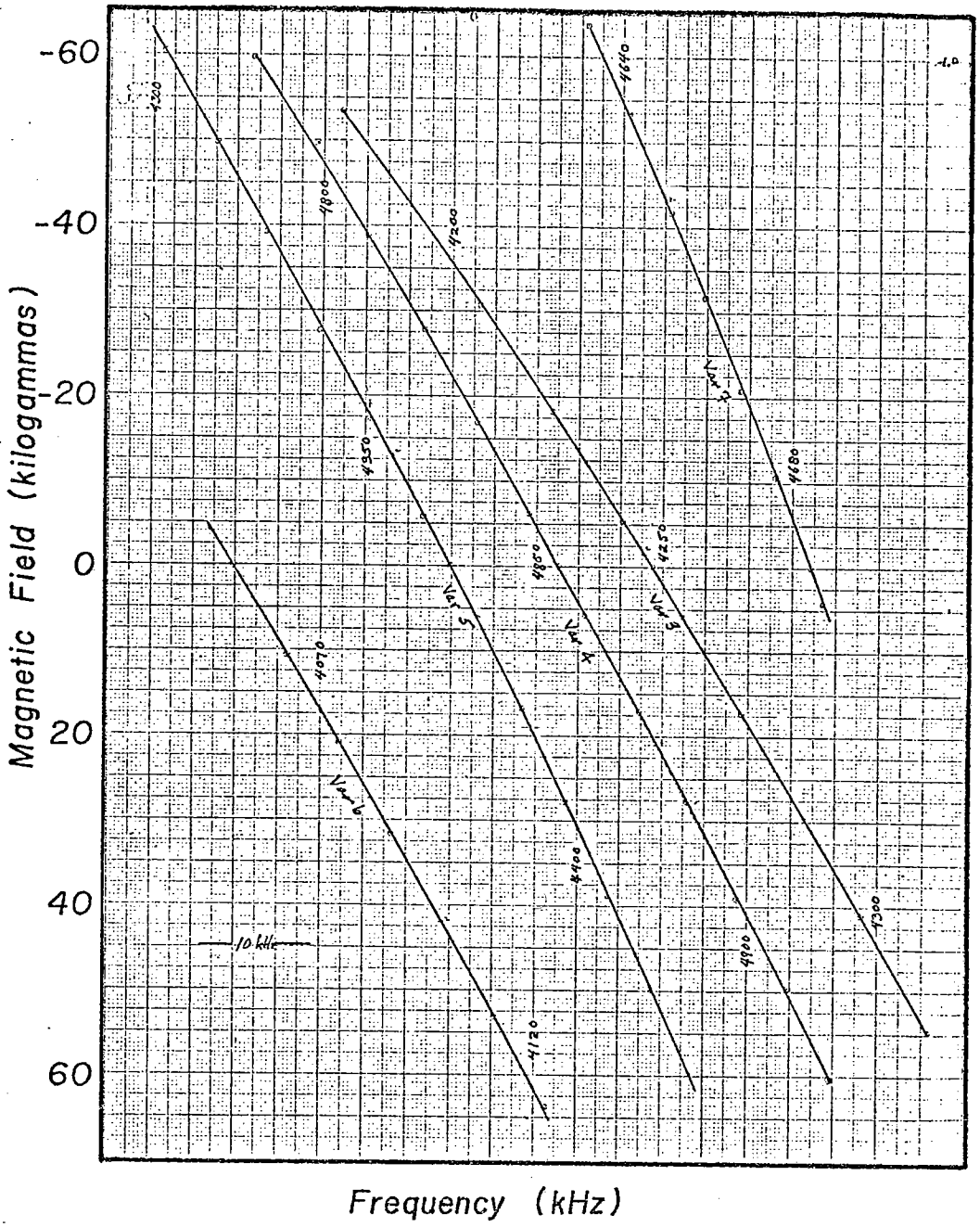

Figure 2.2 Sensor calibration curves (magnetic field versus frequency) for the 1973 instrument. Heavy vertical graph lines are at intervals of 10 kHz. Variables 6 and 7 are vertical axes. Variables 3,4, and 5 are horizontal axes with 4 and 5 oppositely polarized. Frequencies for individual variables are next to their respective plot.

instrument are shown in Figure 2.2. The important feature in the curves is their nearly constant slopes. It is the determination of the slope at a particular field value that is used to convert the recorded frequency to gammas. Again, the calibration is quite reproducible. The 1973 instrument was calibrated before and after deployment; the two calibrations matched to within 1%.

Figure 2.3 shows part of the raw data collected on the seafloor in 1973. Various forms of instrument noise and drift are evident in the plot. The instruments require several days to initially stabilize. The temperature time constant for the instrument is less than 12 hours, so explanations other than temperature must be sought for this initial drift. After the initial stabilization, the instrument exhibits a very long period, slightly non-linear drift.

Oppositely polarized sensor records can be added to eliminate coherent and in-phase signals. Figure 2.4 shows the results of such a calculation using the vertical field records from DA#3 (see Table 3.3). The resulting signal is not necessarily representative of the true noise spectrum. The "noise" calculated by this method can arise in various ways. 1) The large temperature coefficients of the sensors suggest that much of the longer period noise (greater than

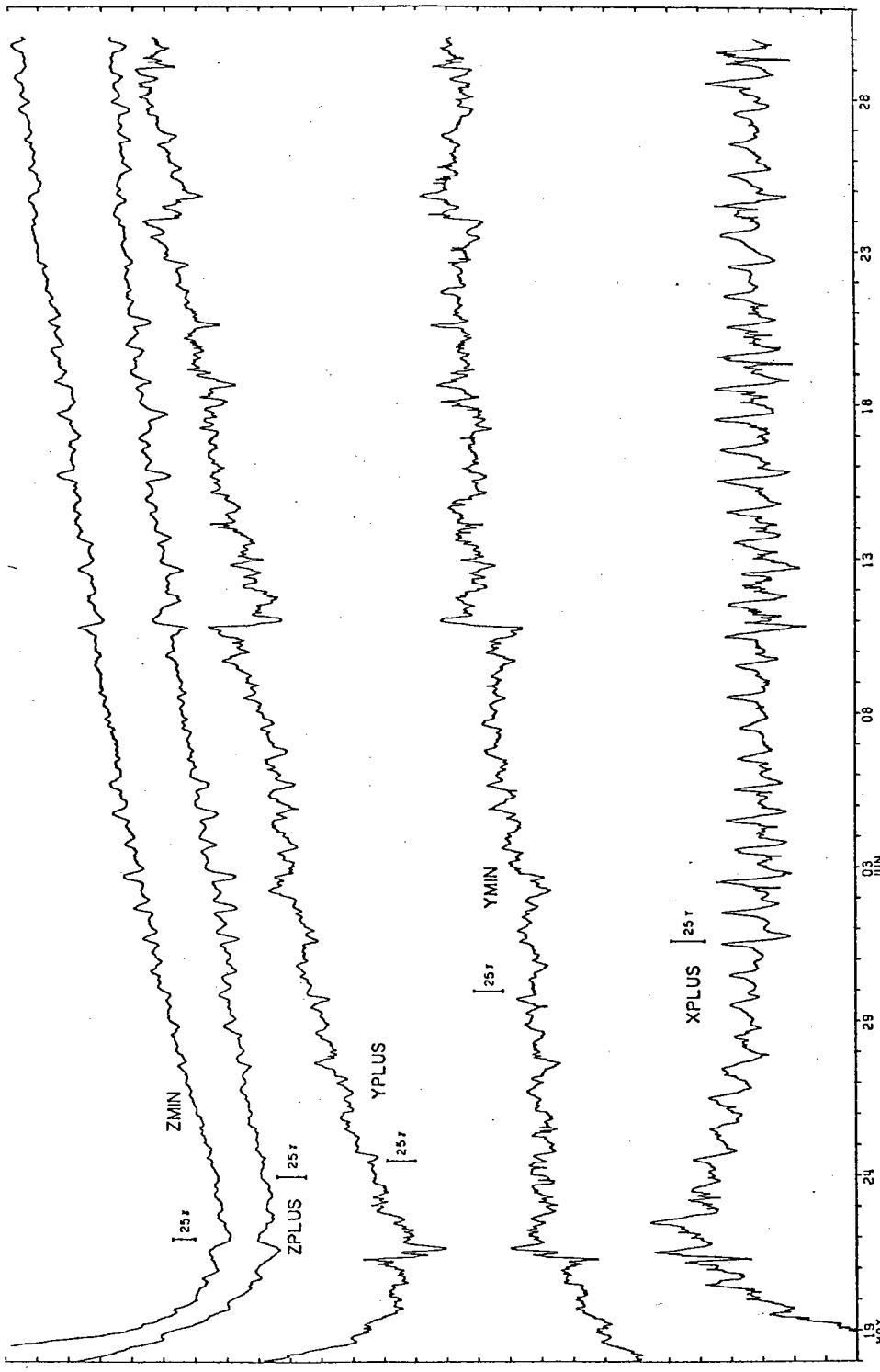

Figure 2.3 Plot of subsampled raw data from SF3. ZPLUS and ZMIN are from oppositely polarized vertical axes; YPLUS and YMIN are from oppositely polarized horizontal axes; XPLUS is orthogonal to YPLUS.

about 8 hours) might be accounted for by temperature fluctuations on the seafloor. This is especially true at the semi-diurnal tidal frequency. Temperature fluctuations to several hundredths of a degree (equivalent to several gammas) are observed on the seafloor during MODE (Brown, 1973). The 1973 temperature sensor recorded similar temperature variations but also recorded other larger amplitude signals. 2) Inaccurate sensor calibration is likely to produce noise that is coherent with the true signals. Little noise of this sort is evident except during the largest of events suggesting good calibrations. 3) The remainder of the noise must be caused by random sensor errors and drift.

It is very difficult to separate the different noise contributions, but much of the longer period noise seems to be attributable to temperature fluctuations. As can be seen from Figure 2.4, signals equivalent to 10 gammas can arise from such fluctuations and must be removed before the data is analyzed. Noise with frequencies above 6 cycles/day has amplitudes ammounting to about 10% of the true signal during active periods. This noise is likely to represent the true sensor noise level and puts a lower limit of about 10 gammas on the amplitude of magnetic events that can be used for analysis. At periods longer than 2 days the computed noise amplitudes are often as large as the signal amplitudes. Removal of the

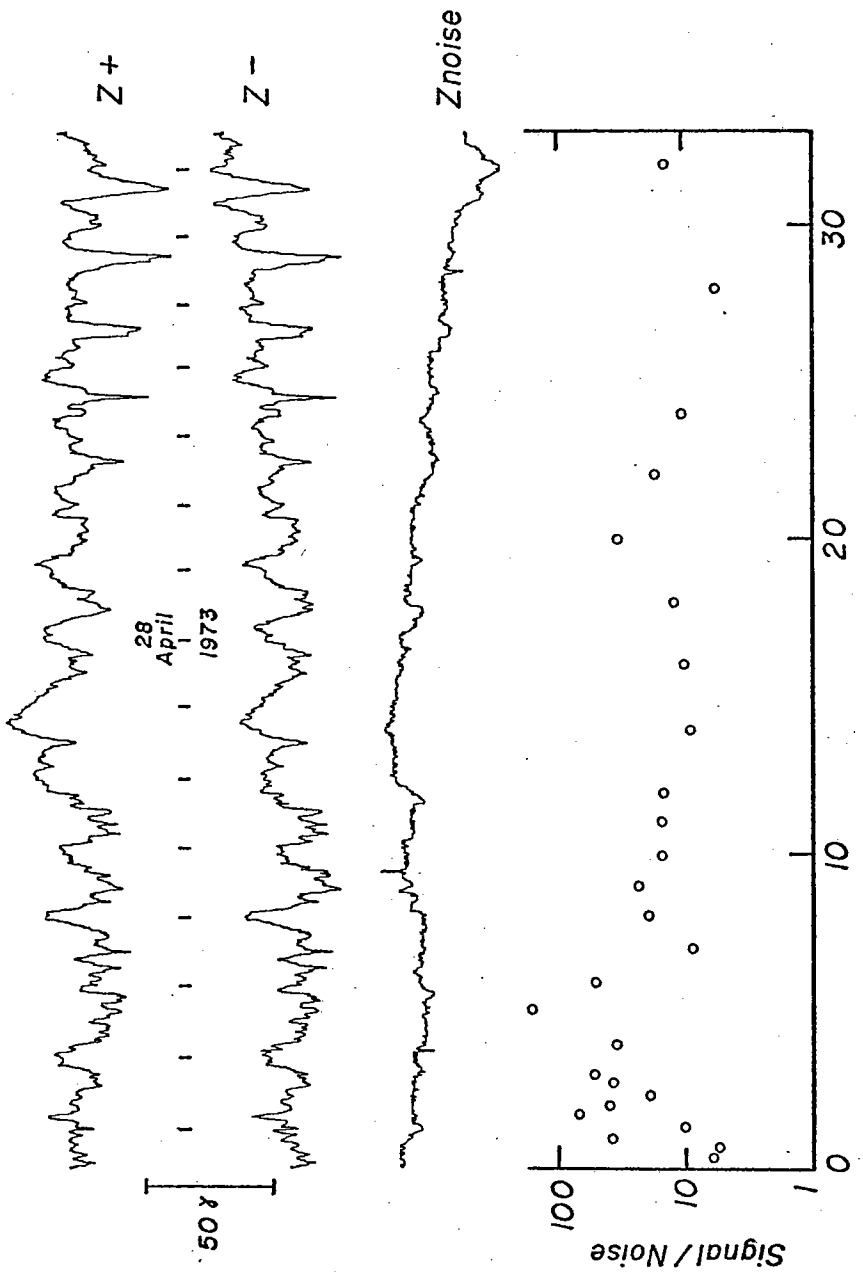

Figure 2.4 Temperature and noise contributions from record section DA#3. Upper two traces are back-to-back vertical components. Znoise is the difference between the vertical component traces. Signal-to-noise ratio is the ratio of the average signal amplitude in Z+ and Z- to Znoise.

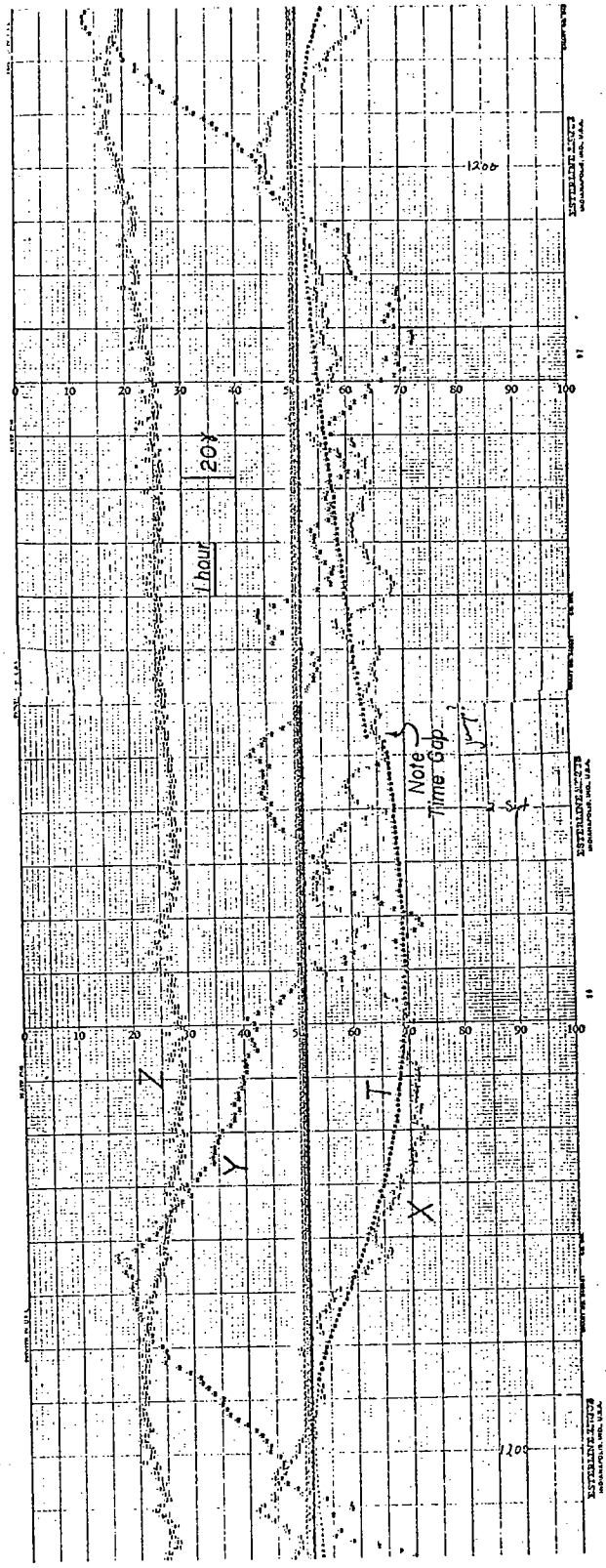

Figure 2.5 Sample magnetogram from 1974 Bermuda land station.

temperature contribution undoubtedly improves this situation, but the large scatter in field ratios obtained for periods longer than 2 days indicates that the remaining long period noise is comparable in amplitude to the signal.

2.2 BERMUDA LAND MAGNETOMETER

During the 1974 field experiment a portable magnetometer was in operation at the Bermuda Biological Station. The instrument was a MFO-3 Fluxgate Magnetometer borrowed from Dr. Roy Hyndman at Dalhousie Institute. The magnetometer was set up in a banana grove as far from disturbing effects as possible. The effect of temperature variations was partially reduced by burying the instrument. A thermistor buried with the instrument recorded daily temperature fluctuations of less than 0.5°C; the instrument temperature coefficient is given to be ±0.5 gamma/°C. The long term stability of the instrument is listed as ±1 gamma/24 hours and the indicated noise level is less than 1 gamma.

Data is recorded approximately once every three minutes on a multi-channel strip chart recorder (Fig. 2.5). Magnetic field values are recorded at 20 gammas/inch vertical scale and 1 inch/hour horizontal scale. As analysis progressed it became apparent that the time resolution should be 100%

better. Also, at several points in time the recorder went off scale. A continuous scale recorder would have been a better choice.

Both the instrument and recorder were powered using external line power. Frequent power failures resulted in numerous short data gaps. Since some of the gaps are short in duration (less than 5 minutes) they remain undetected in the data. Undetected data gaps cause timing errors and reduce coherency with other stations. A backup power supply at least for the recorder would be useful in recording data gaps.

2.3 GEOMAGNETIC OBSERVATORIES

Magnetograms from the Fredericksburg, Virginia and San Juan, Puerto Rico observatories are also used for reference. Data were obtained in the form of normal magnetograms (Fig. 2.6) which include declination, and horizontal and vertical field amplitudes. One day's data represent approximately 18 inches. As with the Bermuda data, this greatly limits the time resolution. The copying process used on the magnetograms further complicates the time base by stretching part of the magnetogram. In places, the time is noted as

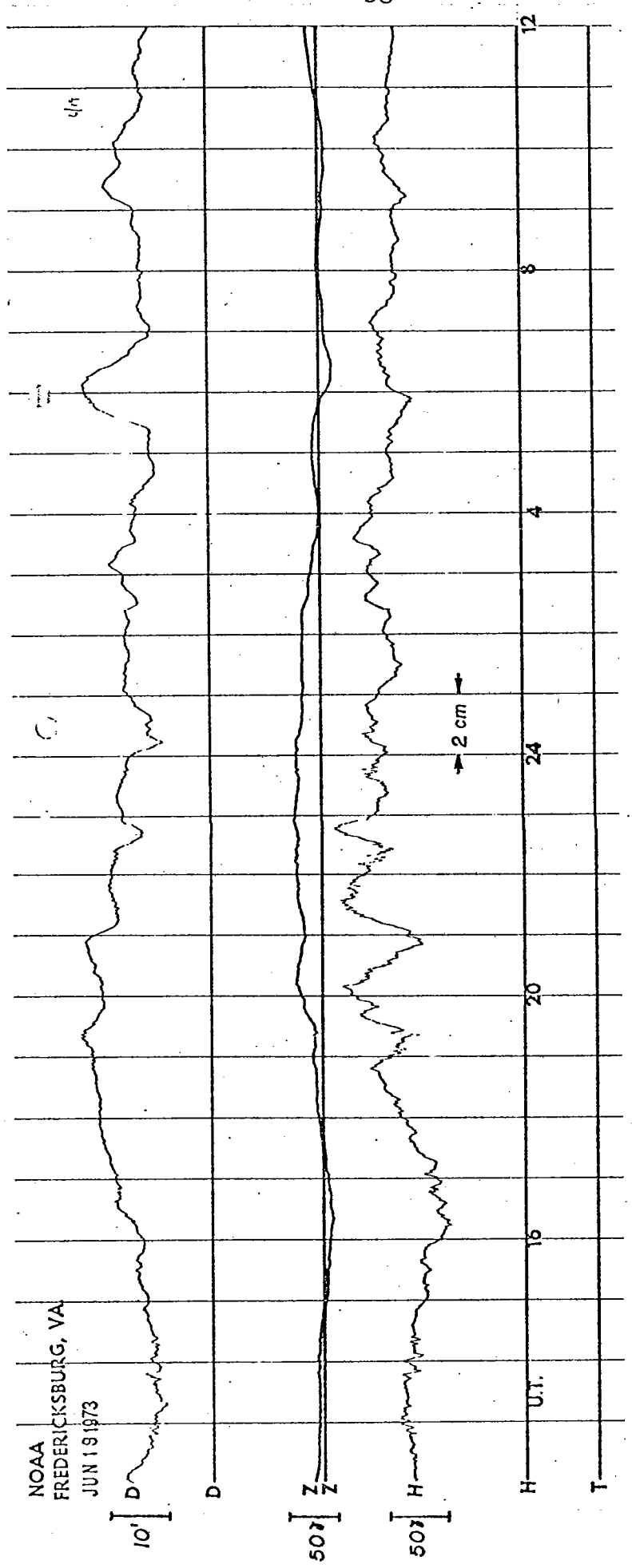

Figure 2.6 Sample magnetogram from geomagnetic observatory at FRV.

being incorrect but no indication of the exact error is given. "Fast run" magnetograms would have provided a more accurate time base but have made the task of digitizing interminable.

CHAPTER III

DATA REDUCTION AND ANALYSIS

3.1 DATA PREPARATION

Chapter II presented most of the data preparation problems. For seafloor instruments it was shown that temperature and drift require attention. Temperature effects have been removed from most data sections (except part of SFA where instrument malfunction occurred) by adding the signals recorded by back-to-back sensors. The frequency of both sensors increases with decreasing temperature, but since the sensors measure oppositely polarized fields the addition of the recorded signals will eliminate the temperature contribution while doubling the field value. This procedure effectively increases the signal-to-noise ratio by better than $\sqrt{2}$.

Except for data sections immediately following the deployment it was sufficient to eliminate the instrument drift by visually removing a linear trend. Immediately following the drop, the data was detrended using the best fit second-order polynomial. In all cases, the mean was subtracted from the data section before it was transformed.

Two other data problems arose: 1) one sensor had a tendency to randomly jump at infrequent intervals, and 2) the SFA instrument malfunctioned by recording spurts of spurious

values (it eventually became too bad to correct). The first problem was easily dealt with by simply determining where a jump occurs and subtracting the value of the jump from all following data. Since all the jumps were larger than the point-to-point signal changes, they could be easily recognized and totally eliminated. The second problem was more difficult to handle and in actuality could only be remedied in a few situations. A linear trend was calculated using several adjacent good points. The following point was compared to the value predicted by the trend and was either accepted if it falls within 5 gammas of the prediction or rejected. If accepted, a new trend was calculated. If rejected, the next point was compared until an acceptable point was found. The effectiveness of this routine is dependent upon two things: 1) how many consecutive bad points are found, and 2) how much the true value deviates from the linearly predicted value. Taking the two constraints together it was found that only quiet time magnetic variations with data gaps of less than about 10 minutes (10 points) could be totally corrected. As more real magnetic activity appeared on the record the method could only correct for 2-3 consecutive bad points. After all the bad points are removed, an interpolation routine recreates a smoothed version of the original time series from the "good

points". Only the first of three months of data were useful in this study.

Reference station magnetograms were hand digitized onto magnetic tape using a Bendix Datagrid Digitizer. The digitizing interval varied from 2.5-10.0 minutes depending on the use of the data. The tape values were reformatted for computer compatibility onto another magnetic tape and plotted to check for inaccuracies. Deviations of the digitized trace from the original trace are less than 0.5 gamma and are not a factor in the analysis.

3.2 DATA ANALYSIS

The discussion of the vertical gradient of horizontal fields method in Section 1.3 shows that the transfer function between the seafloor and seasurface magnetic field values (R) is the basis of analysis. The electromagnetic impedance is easily calculated from these transfer functions. Data analysis is carried out in four steps: 1) estimation of the seasurface magnetic variations, 2) calculation of the transfer function for individual events, 3) smoothing and averaging the transfer functions and 4) calculation of the apparent resistivity and phase for each magnetometer site.

Surface field estimation

Of the four steps, the most difficult to accurately accomplish is the first-estimation of the surface field. The source fields dealt with in this study are of three types: 1) the Sq field, 2) the geomagnetic storm field, and 3) the polar substorm field.

The Sq variation field is caused by tidally and thermally generated winds in the ionosphere (Chapman, 1964). The Sq current system remains nearly fixed relative to the sun but does show some seasonal variation (Matsushita, 1967; Chapman and Bartels, 1940). Spherical harmonic analyses reveal that the Sq field and its first three harmonic frequencies can be adequately represented by a single spherical harmonic term at each frequency (Suzuki, 1973; Matsushita and Maeda, 1965). The amplitude and phase of the Sq field is observed to vary slowly (decreasing southward) at middle dip-latitudes. However, Suzuki (1973) predicts a smaller decrease in amplitude than Matsushita and Maeda (1965).

Since magnetic observatories in the oceans tend to be sparse, a small cursory study of the Sq variations was undertaken using the magnetometer stations at FRV, SJP, MHB, and BER. The relative amplitudes and phases between BER and MHB (Table 3.1) indicate a small latitudinal variation of Sq in

TABLE 3.1 Amplitude and Phase of Diurnal Harmonics

Section	T	Y_{SF}	Y_{SFA}	Y_{SFC}	Y_{FRV}	Y_{BER}	Y_{SJP}	Y_{MHB}
DA#1	24	6.6 257°			14.2 288°	12.1 273°		11.4 275°
DA#2	24	8.9 140°			15.9 188°		17.1 310°	16.3 156°
DA#3	24	6.8 128°			12.4 176°	11.5 158°		12.2 137°
DA#4	24		8.9 296°	9.6 301°		20.5 326°		
DA#5	24			10.0 310°		22.9 322°		
DA#6	24		2.3 98°			7.6 122°		
DA#7	24		6.15 289°	6.81 284°		14.0 306°		
DA#1	12	3.0 8°			7.1 26°	5.7 25°		5.3 15°
DA#2	12	3.7 131°			7.1 185°		6.4 123°	7.3 134°
DA#3	12	3.2 70°			6.3 117°	6.0 107°		6.0 55°
DA#4	12		4.4 79°	4.9 77°		8.4 101°		
DA#5	12			6.0 52°		11.4 66°		
DA#6	12		5.0 35°			10.0 66°		
DA#7	12		5.8 22°	6.1 4°		11.9 33°		
DA#1	8	1.1 123°			2.6 127°	2.3 144°		1.2 22°
DA#2	8	1.8 133°			2.04 223°		2.8 124°	2.6 136°
DA#3	8	1.0 52°			2.0 130°	1.9 80°		2.1 129°
DA#4	8		2.1 220°	2.4 206°		3.9 249°		
DA#5	8			2.0 178°		3.6 191°		
DA#6	8		3.4 345°			5.6 338°		
DA#7	8		3.3 132°	4.1 105°		7.4 145°		

All phases are relative to Bermuda instrument location and time.
Amplitudes are in gammas.
Period (T) is in hours.
Dates of data sections are listed in Table 3.2.

this part of the North Atlantic. Amplitude decreases less than 5% for all harmonics between BER and MHB but the phase changes are not regular, and may be affected by the proximity of MHB to the coast. Since all seafloor Sq variations will be referenced to BER, it appears unnecessary to correct for the small latitudinal differences.

Geomagnetic storms are caused by the impact of solar plasma on the earth's magnetic field (Chapman, 1964). Current flows are enhanced in the auroral electrojets and westward Ring current. The onset of a storm is nearly globally simultaneous, but the morphology of the storm may significantly change with location (Chapman and Bartels, 1940).

Polar substorms are believed to be caused by the injection of high energy into the nightside magnetosphere (Rostoker, 1972; Clauer and McPherron, 1974a,b). The intensification of the electrojets is limited to 10-90° of longitudinal spread but may occur anywhere between the dawn and dusk meridian. The morphology of the perturbation field is spatially dependent.

Polar substorms may occur as isolated events or in large numbers during geomagnetic storms. Porath et al (1971) have estimated apparent wavelengths for substorms to be 5000-10000 km within their arrays. Wavelengths of 10000-20000 km have been estimated in a similar manner (wavenumber $k = |\partial H/\partial x|/|H|$

wavelength = $2\pi / k$) from the reference station data. Amplitude ratios for three period bands (4-2 hrs, 2-1 hrs, 1-0.3 hrs) are compared for five storms at FRV, SJP, and BER. Average relative amplitudes for each band are listed in Table 3.2. Ratios vary considerably more between bands for FRV/SJP, possibly due to the low magnetic latitude of SJP. At times, bays at SJP appear to be greatly out of phase relative to FRV indicating magnetic influences from the southern hemisphere or the equatorial electrojets. On this basis, the more consistent data from FRV/BER are used to calculate a wavenumber. The nearly equal ratios for both field components and all three bands implies one wavenumber equal to 0.0003 km^{-1} is sufficient. Source fields for periods longer than 4 hours have even smaller wavenumbers and will not be corrected for latitude.

Estimation of cross-spectra

As shown in Section 1.3 the basic data parameter for any type of analysis is the scalar or tensor transfer function between measured magnetic fields or electric and magnetic fields. An estimate of this transfer function is obtained from the appropriate cross-spectra, whether band averaged or not.

TABLE 3.2 Band-averaged Magnetic Field Ratios for Wavelength Estimates

Band (hrs)	X_{FRV}/X_{SJP}	Y_{FRV}/Y_{SJP}	X_{FRV}/X_{BER}	Y_{FRV}/Y_{BER}
4. - 2.	1.4	5.0	1.2	1.1
2. - 1.	1.9	2.5	1.3	1.3
1. - 0.3	2.9	2.8	1.3	1.0

N-S distance between FRV and SJP is about 2000 km

N-S distance between FRV and BER is about 600 km

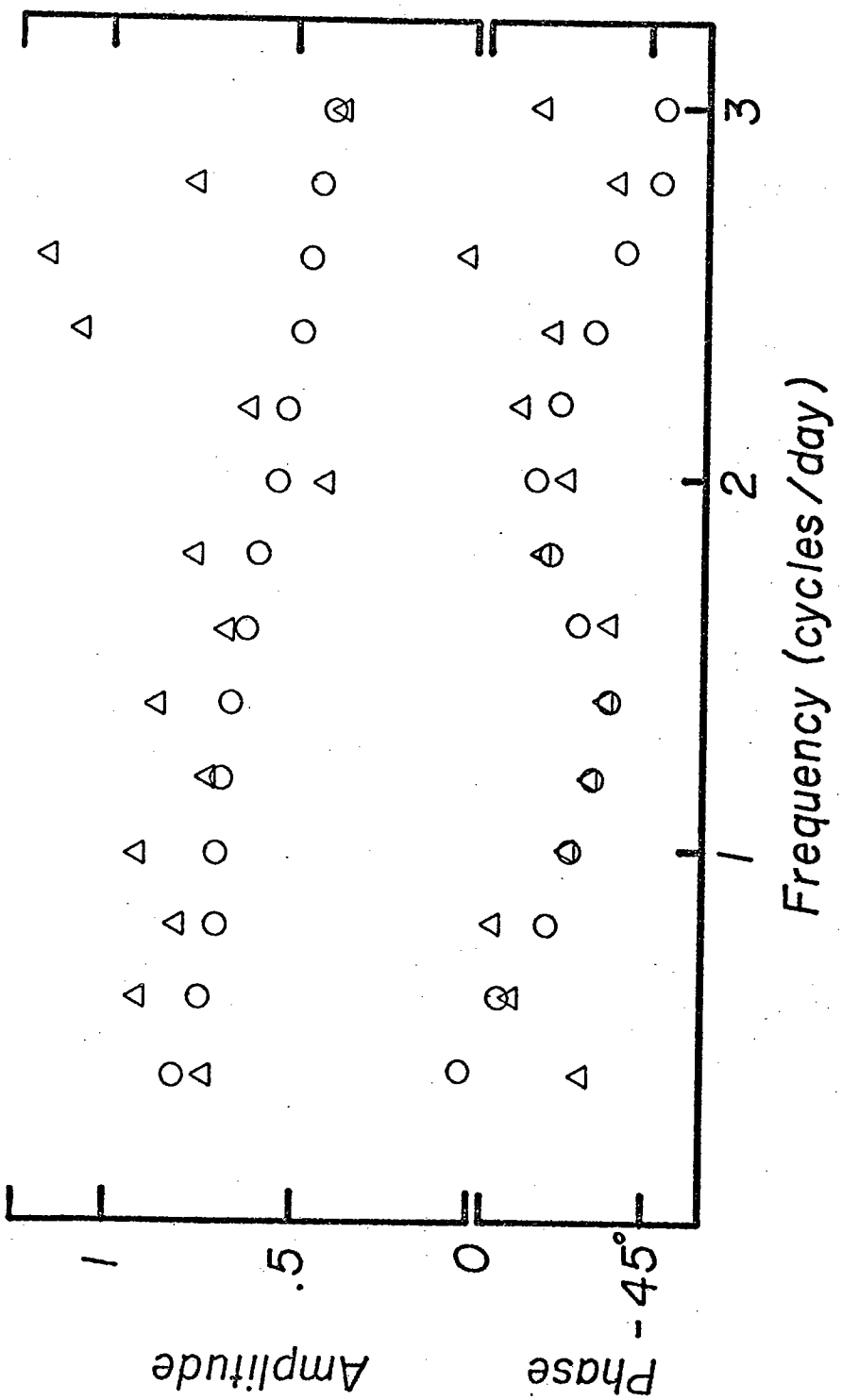

Figure 3.1 Comparison between long period maximum likelihood transfer functions (circles) and those calculated from fast Fourier transforms (triangles).

Traditionally, cross-spectra have been estimated from either the Fourier transform of the correlation function or more directly from the Fourier transforms of the individual time series. Both methods involve the use of some form of windowing. The latter method will be used in this study.

After prewhitening (first difference high-pass filtering), the cross-spectra become

$$C_{12}(f_k) = \sum_{j=k-m/2}^{k+m/2} X_1(f_j) X_2^*(f_j) H_{k-j}$$

where H(f) is a window of bandwidth m. In actuality, averaging can be between different records or within a single record as long as the spectra are smoothly varying. The averaging window is used to give statistical stability to the estimate. The use of a fast Fourier transform to estimate the periodogram results in contamination of individual frequency estimates by neighboring frequencies, especially if the neighboring value is large. Frequency band averaging tends to compensate for this contamination by including more signal in each averaged estimate.

Maximum likelihood cross-spectral estimation (Lacoss, 1971) eliminates much of the statistical instability of the Fourier transform (Fig. 3.1). The cross-spectra are treated as the cross correlation of the frequency content of the time

series. This method estimates the frequency content of each time series by designing a filter that minimizes the interference between neighboring frequencies in the maximum likelihood sense (Lacoss, 1971; Baggeroer, 1975). This filter is thus data dependent so that the quality or resolution of the filter depends on the quality as well as the length of the data (Lacoss, 1971). Potentially narrower frequency bands can be resolved and the utilization of the statistical properties of the data largely removes the need for band averaging.

3.3 DIURNAL ANALYSIS

Magnetograms (Figs. 3.2 and 3.3) from geomagnetically quiet periods are strongly dominated by the solar diurnal harmonics and the lunar semi-diurnal harmonic. These signals change little from day to day during quiet periods and hence may be modeled as deterministic. Spectral analysis is therefore concerned with the estimation of a regular signal composed of several distinct frequencies (f_i) superimposed upon random Gaussian noise.

If a periodogram analysis is performed one measures the sum of the signal and noise

$$X'(f_i) = X(f_i) + N(f_i) \ .$$

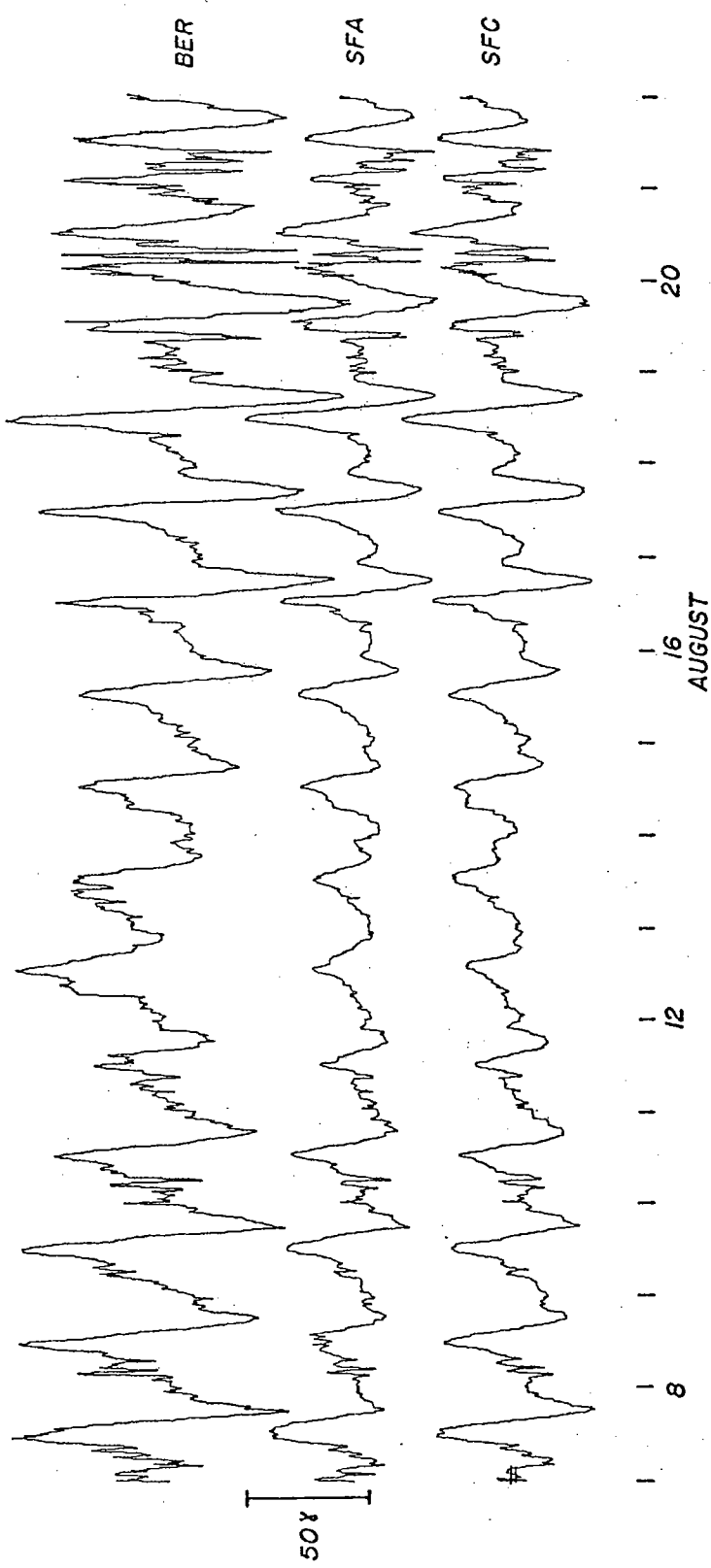

Figure 3.2 Fifteen-day quiet magnetograms from seafloor and reference stations.

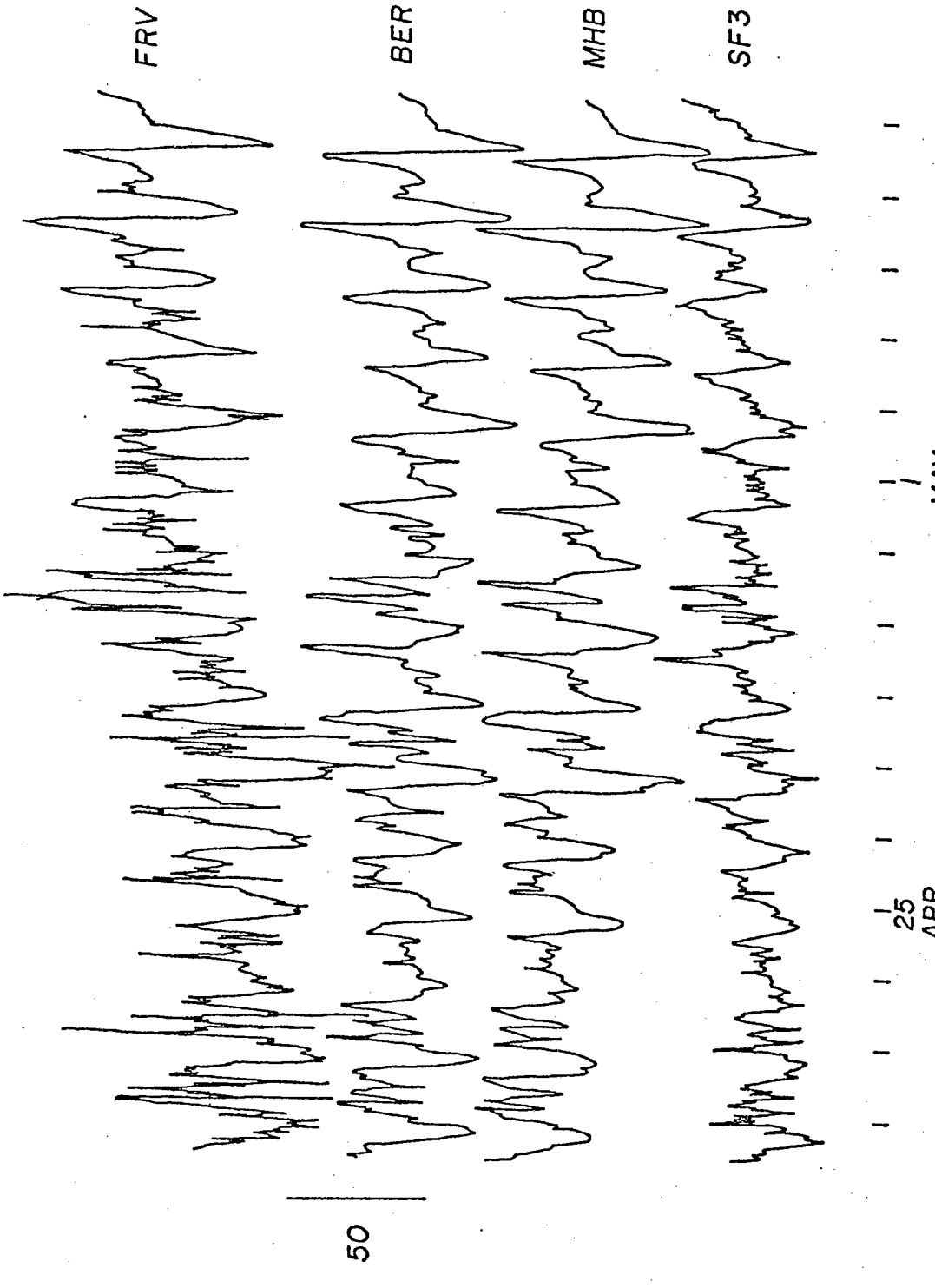

Figure 3.3 Fifteen-day quiet magnetograms from seafloor and reference stations.

The noise component ($N(f_i)$) can be accurately determined from neighboring frequency bands by band-averaging so that

$$\langle X'(f_i) \rangle = X(f_i)$$

and

$$\text{var } (X(f_i)) = C_{NN}(f_i)$$

where C_{NN} is the power contained in the background noise. This means

$$|X'(f_i)| \cong |X(f_i)| \pm \alpha$$

$$\arg(X'(f_i)) \approx \arg (X(f_i)) \pm \beta$$

where

$$\alpha = (C_{NN}(f_i))^{1/2};$$

$$\beta = 1/2(\tan^{-1}(b/a + \delta) - \tan^{-1}(b/a - \delta));$$

$$\delta = \alpha/2a^2 |X'(f_i)|$$

and

$$X'(f_i) = a + ib \text{ (Greenhouse, 1972).}$$

The long period spectrum during quiet times is dominated by the solar diurnal harmonics (S_1, S_2, S_3 and sometimes S_4) but may also have a strong contribution from the lunar semi-diurnal variation M_2 (12.4206 hour period) in oceanic regions. In this study, as well as in previous analyses (Larsen, 1968), this was found to be true. Figure 3.4 shows the amplitude spectra from a 15-day record of relatively quiet variations.

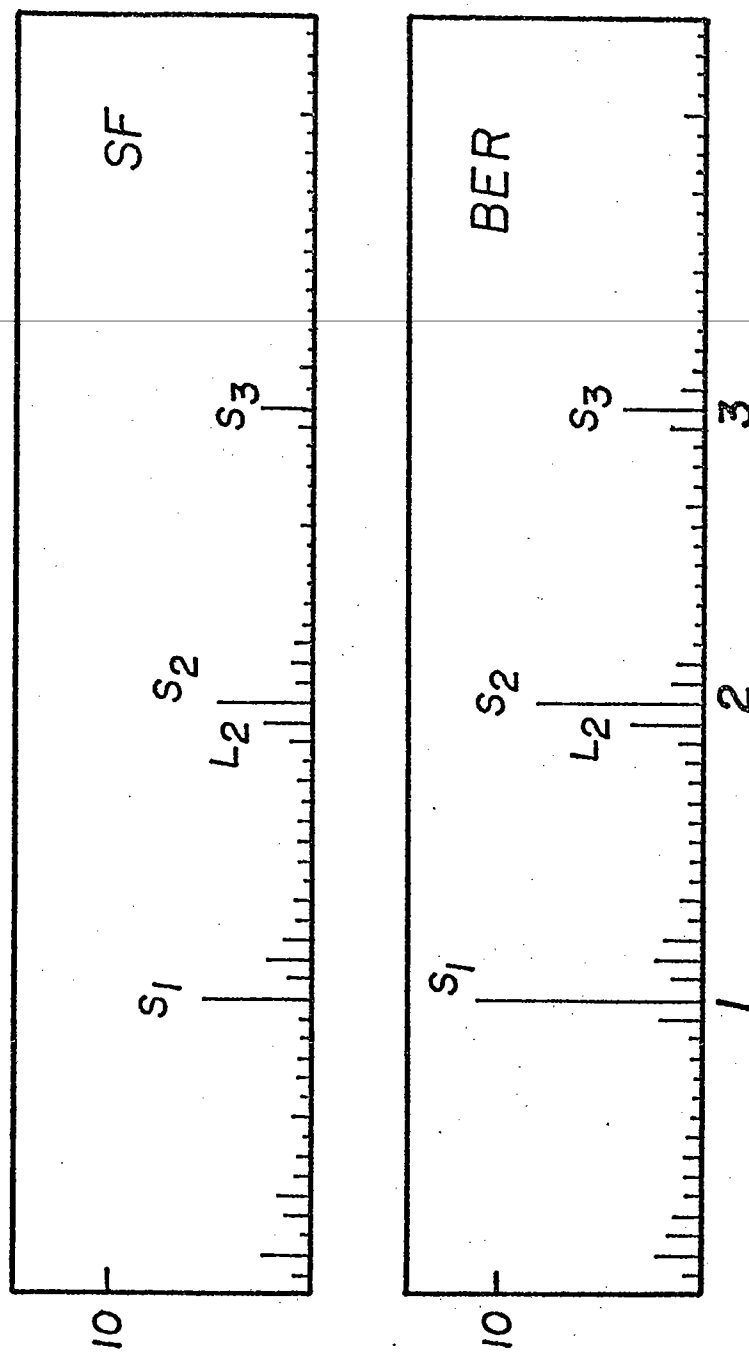

Figure 3.4 Long period amplitude spectra from DA#1. Vertical scale is in gammas.

The amplitude of M_2 is nearly half that of S_2 both on Bermuda and the seafloor. The amplitude of S_4 is not significantly above the background noise level at any site. With this possible error in mind, it becomes necessary to analyze record sections at least 15 days long to obtain uncontaminated diurnal harmonics. Unfortunately this eliminates the opportunity to average results from numerous record sections.

Magnetic field ratios between the seafloor and seasurface are presented in Figure 3.5 for the three sites. Ratios for the first three diurnal harmonics are calculated from the amplitude and phase spectra for several data sections (Table 3.3) and then averaged. Ratios for SF are shown referenced both to FRV and BER. The BER variations are uncorrected for latitudinal changes. Although the average amplitude ratios are comparable, there is considerable disagreement in the phase results which might indicate source field variation. Phase differences between FRV and BER or MHB are large and inconsistent compared to those between BER and MHB which have been shown to be negligible. Since FRV gives inconsistent results and is a great distance from SF, the ratios referenced to BER are used for station SF. This choice also means that all sites are referenced to a common station for the diurnal harmonics.

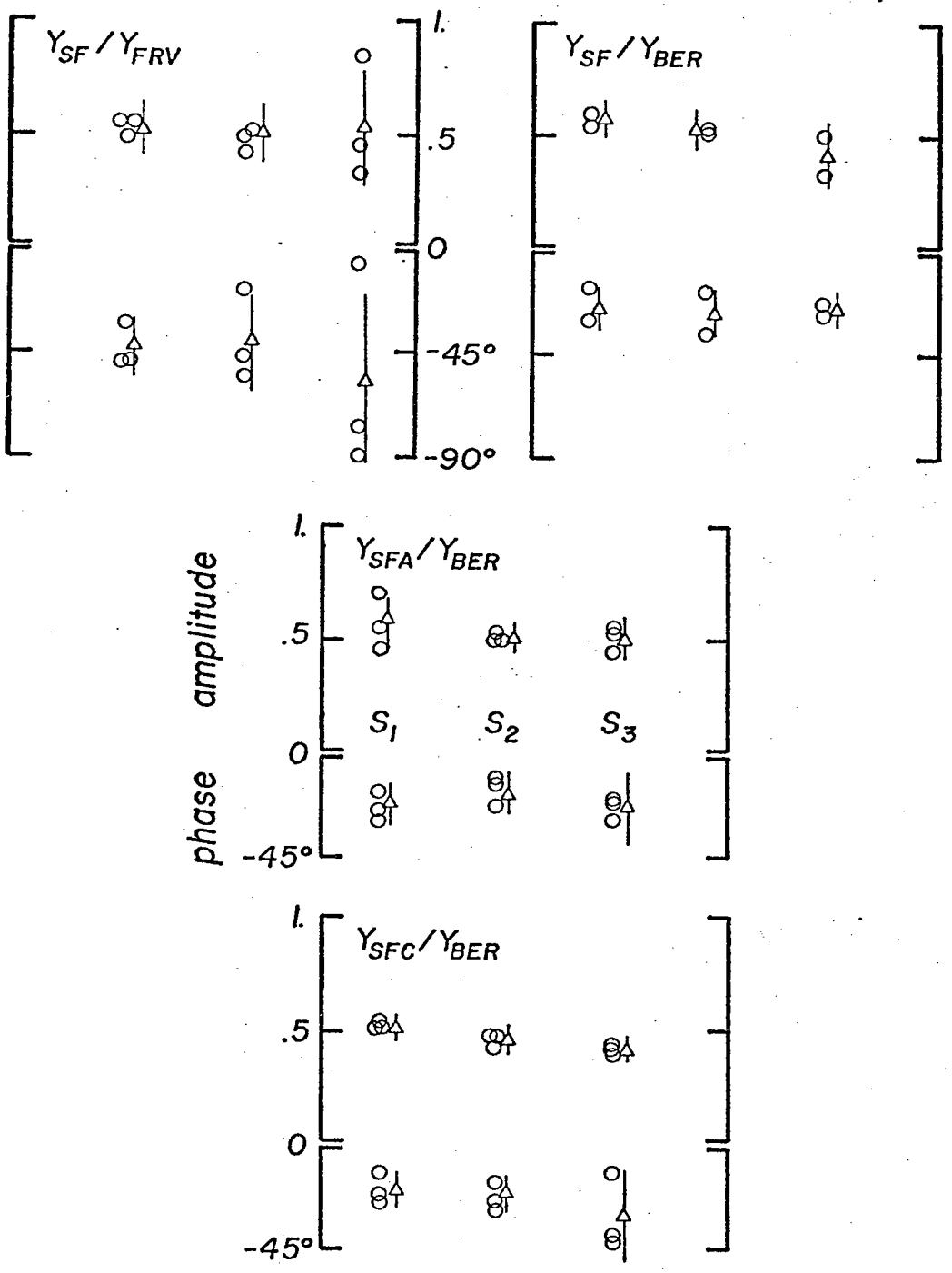

Figure 3.5 Individual (circles) and average (triangles) transfer functions for the diurnal harmonics at each sea-floor site. Error bars represent the 95% confidence limits.

Table 3.3

Data sections used in diurnal analyses

Section	Date	Stations
DA#1	7305232207 - 7306072207 Z	SF3,FRV,BER,MHB
DA#2	7306131411 - 7306281411 Z	SF3,FRV,SJP,MHB
DA#3	7304211241 - 7305061241 Z	SF2,FRV,BER,SJP,MHB
DA#4	7408070000 - 7408220000 Z	SFA,SFC,BER
DA#5	7408270000 - 7409110000 Z	SFC,BER
DA#6	7408240606 - 7408290606 Z	SFA,BER
DA#7	7409052300 - 7409102300 Z	SFA,SFC,BER,FRV

Table 3.4

Data sections used for active record analyses

Section	Date	Stations
AA#1	7306100000 - 7306150000 Z	SF3,FRV,SJP
AA#2	7305210005 - 7305220005 Z	SF3,FRV,SJP
AA#3	7304121200 - 7304171200 Z	SF2,FRV,SJP
AA#4	7303311200 - 7304051200 Z	SF2,FRV,SJP
AA#5	7409150000 - 7409200000 Z	SFC,BER,FRV
AA#6	7410080000 - 7410160000 Z	SFC,BER,FRV
AA#7	7304160000 - 7304240000 Z	SF2,FRV,SJP
AA#8	7408181200 - 7408231200 Z	SFA,SFC,BER
AA#9	7409240000 - 7410010000 Z	SFC,BER,FRV

3.4 CONTINUUM ANALYSIS

Continuum transfer functions are estimated from the cross-spectra using both a scalar and tensor analyses. The tensor transfer functions can be written in the frequency domain as

$$x = A_{xx}X + A_{xy}Y$$
$$y = A_{yx}X + A_{yy}Y \qquad \text{Eq. 3.1}$$

where x and y are the magnetic fields at the seafloor, X and Y are those at the surface and the A's are transfer functions. As an example, the first equation can be solved for A_{xx} to give

$$A_{xx} = \frac{\langle xX^* \rangle \langle YY^* \rangle - \langle xY^* \rangle \langle YX^* \rangle}{\langle XX^* \rangle \langle YY^* \rangle - \langle XY^* \rangle \langle YX^* \rangle}$$

The difference between the scalar and tensor analyses can quickly be appreciated. A_{xx} exactly represents its scalar equivalent if and only if $\langle XY^* \rangle = 0$. In general $\langle XY^* \rangle \neq 0$, causing the scalar analysis to show considerably less stability than the tensor. The advantage of the tensor analysis is that after the tensor transfer function elements are calculated they can be rotated using a similarity transformation to find the direction of the most coherent orthogonal magnetic fields. In this "principal direction" the off-diagonal transfer functions will be at a minimum.

Another important consideration is the bias in estimates resulting from noise. The scalar transfer function A_{xx} can be calculated as $\langle xX^* \rangle / \langle XX^* \rangle$ or as $(\langle Xx^* \rangle / \langle xx^* \rangle)^{-1}$. If there is no noise contamination, the two estimates are identical. But in the presence of noise, the former results in $A'_{xx} = A_{xx}/(1 + r)$ and the latter in $A'_{xx} = A_{xx}(1 + r)$ where r is the noise-to-signal ratio. Figure 3.6 illustrates this biasing as well as the effect of using the tensor analysis. Since it is likely that the reference stations have less noise than the seafloor stations, it is more reasonable to choose $\langle xX^* \rangle / \langle XX^* \rangle$ as the best estimate for the transfer function.

Confidence limits for smoothed least squares transfer functions have been estimated from the χ^2_ν property of $\nu \, \bar{C}_{zz}/\Gamma_{zz}$ (where ν is the number of degrees of freedom in the auto- and cross-spectra, $\bar{C}_{zz}$ is the smoothed spectral estimate of the least squares residual and Γ_{zz} is its theoretical estimate)(Jenkins and Watts, 1969; Chap. 10). $(\bar{G})$ and phase (ϕ) is approximated by

$$|\Delta G| \leq k \qquad \sin|\Delta\phi| \leq \frac{k}{\bar{G}}$$

Eq. 3.2

$$\frac{k^2}{\bar{G}^2} = \frac{2}{\nu-2} \; \frac{1 - K_{12}^2}{K_{12}^2} \; f_{2,\nu-2}(1-\alpha)$$

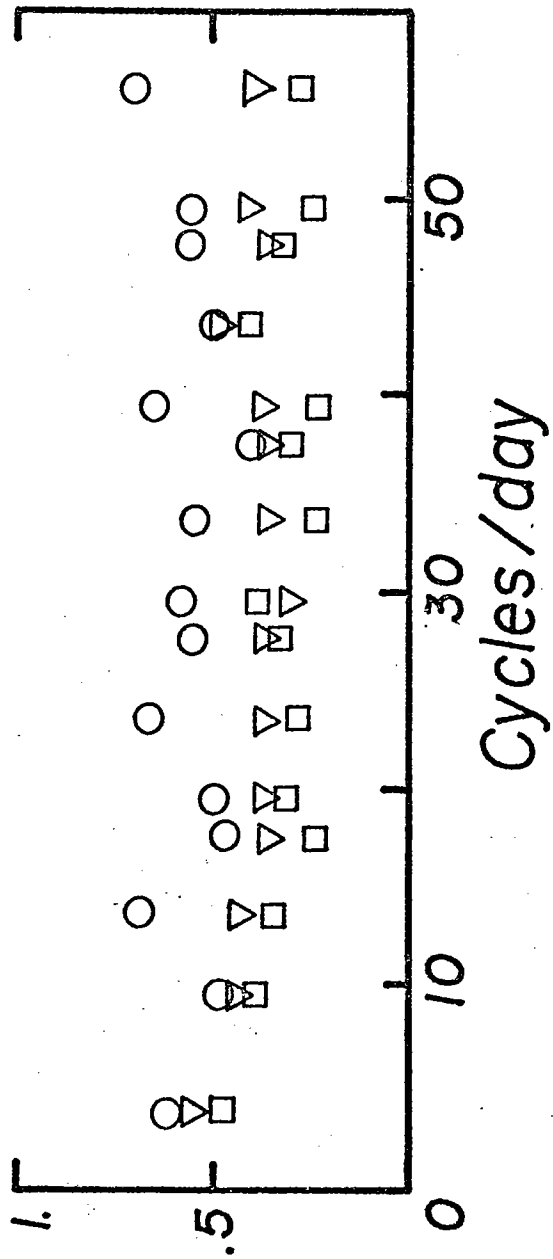

Figure 3.6 Biasing of transfer function estimates. Circles correspond to ($\langle Xx^* \rangle$ / $\langle xx^* \rangle$)-1, squares to ($\langle xX^* \rangle$ / $\langle XX^* \rangle$), and triangles to tensor estimates.

where K_{12} is the coherency and $f_{2,\nu-2}(1-\alpha)$ is the appropriate chi square parameter. For Gaussian statistics the 95% confidence limit is equivalent to two standard deviations. Similar confidence intervals can be calculated for the tensor case (Jenkins and Watts, 1969; Chap. 11).

As can be seen from equation 3.2, the magnitude of the confidence intervals is determined by ν, K_{12} and $f_{\nu,\nu-2}$. For data with good coherence ($K_{12} \geq .85$) the coherence is not a strong function of ν as long as some smoothing is done. $f_{\nu,\nu-2}$ is also not a strong function of ν for ν greater than about 20. So, for relatively large ν the confidence limits are controlled by $1/\nu$, and a good compromise between resolution and variance can be had by using 20-30 equivalent degrees of freedom.

The data sections used in the continuum analysis are listed in Table 3.4. Wherever possible the data is analyzed using both the scalar and tensor analysis. The data can be divided into sections in numerous ways. Some prefer to look at individual events with a limited frequency content while others analyze more lengthy records containing many events of broad frequency content. This study takes the latter approach by utilizing active record sections of 5 and 8 day durations

(Figs. 3.7-3.9). This helps average out the changing source field wavenumbers. A large number of events are thus averaged within each data segment and will later be averaged between segments.

An attempt was made to compare the results obtained from a long (8 day) section with those from several shorter portions of the same section. The shorter portions exhibited varying degrees of scatter about the whole section results, but the mean reproduced the whole section results reasonably well. This type of behavior should be anticipated since the time series are not stationary and the source configuration (hence its spatial variation) may change from event to event. Averaging a large number of slightly different source fields into one estimate tends to make the average source field have a greater apparent uniformity.

Further source field effects can be noticed in the comparison of scalar and tensor transfer functions at SFC (Figs. 3.12A and B). For most events coherence (XY) tends to rise with frequency. As previously discussed this has two effects: 1) the scalar functions become biased upward and are in general less reliable because all contributions are not considered, and 2) the tensor analysis becomes unstable as the requirement

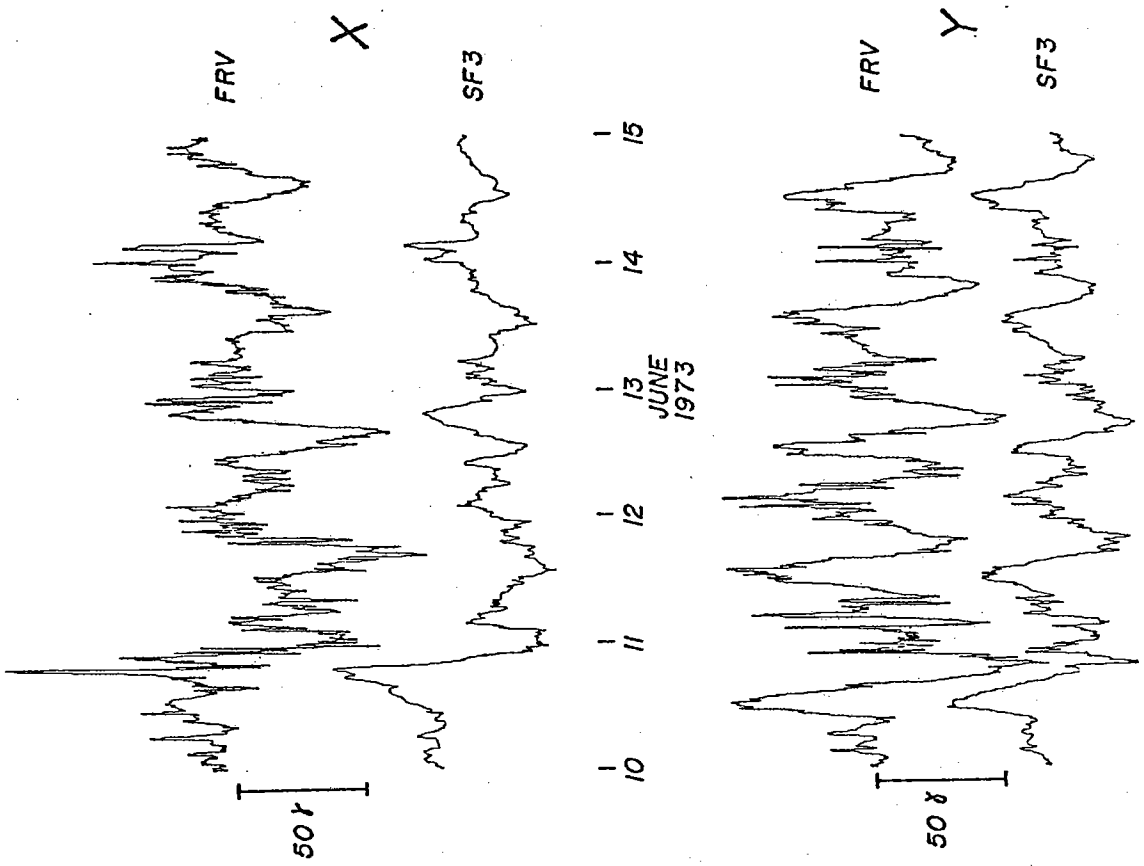

Figure 3.7 Storm and substorm magnetograms from seafloor and reference stations.

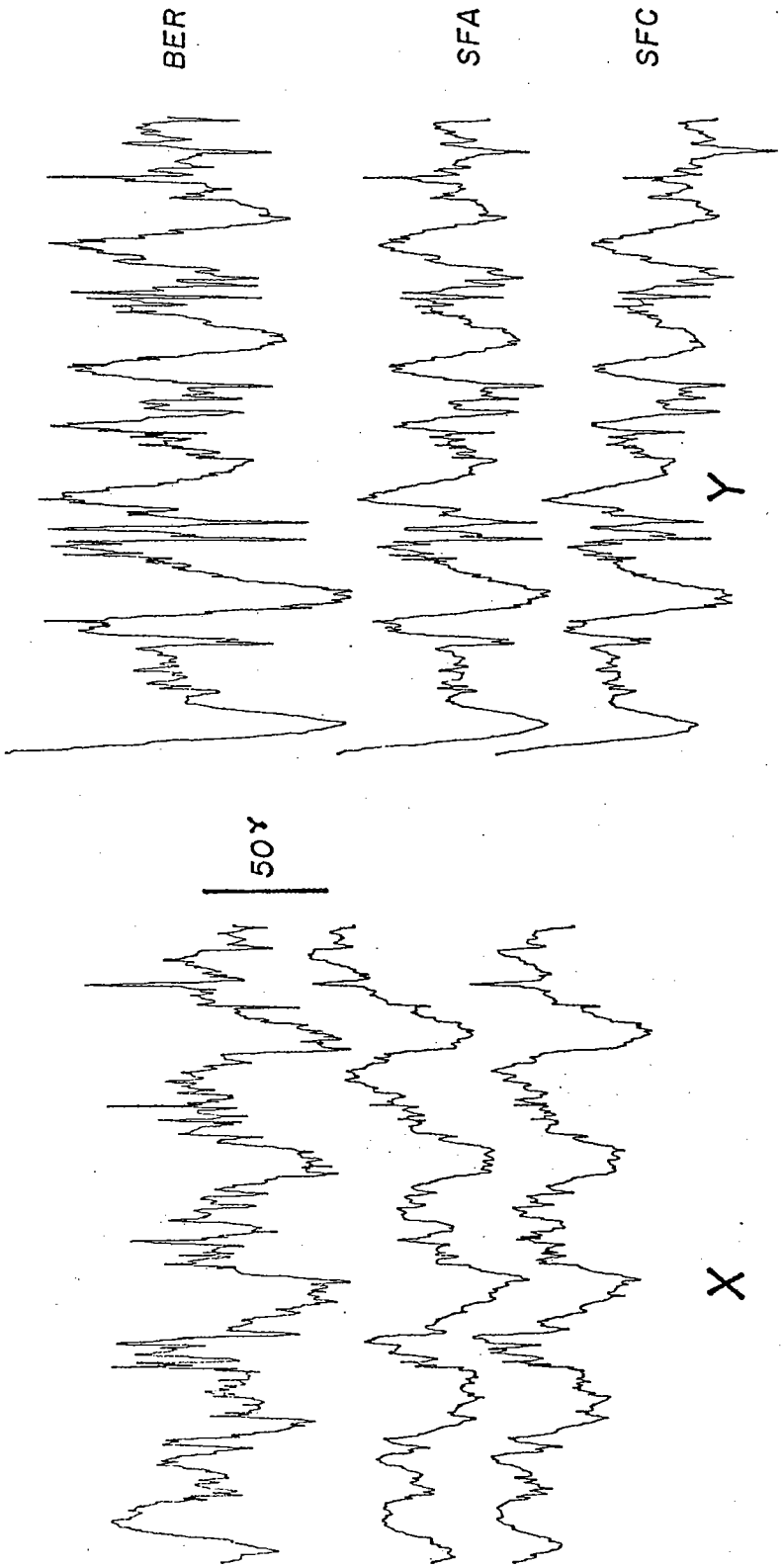

Figure 3.8 Storm and substorm magnetograms from seafloor and reference stations.

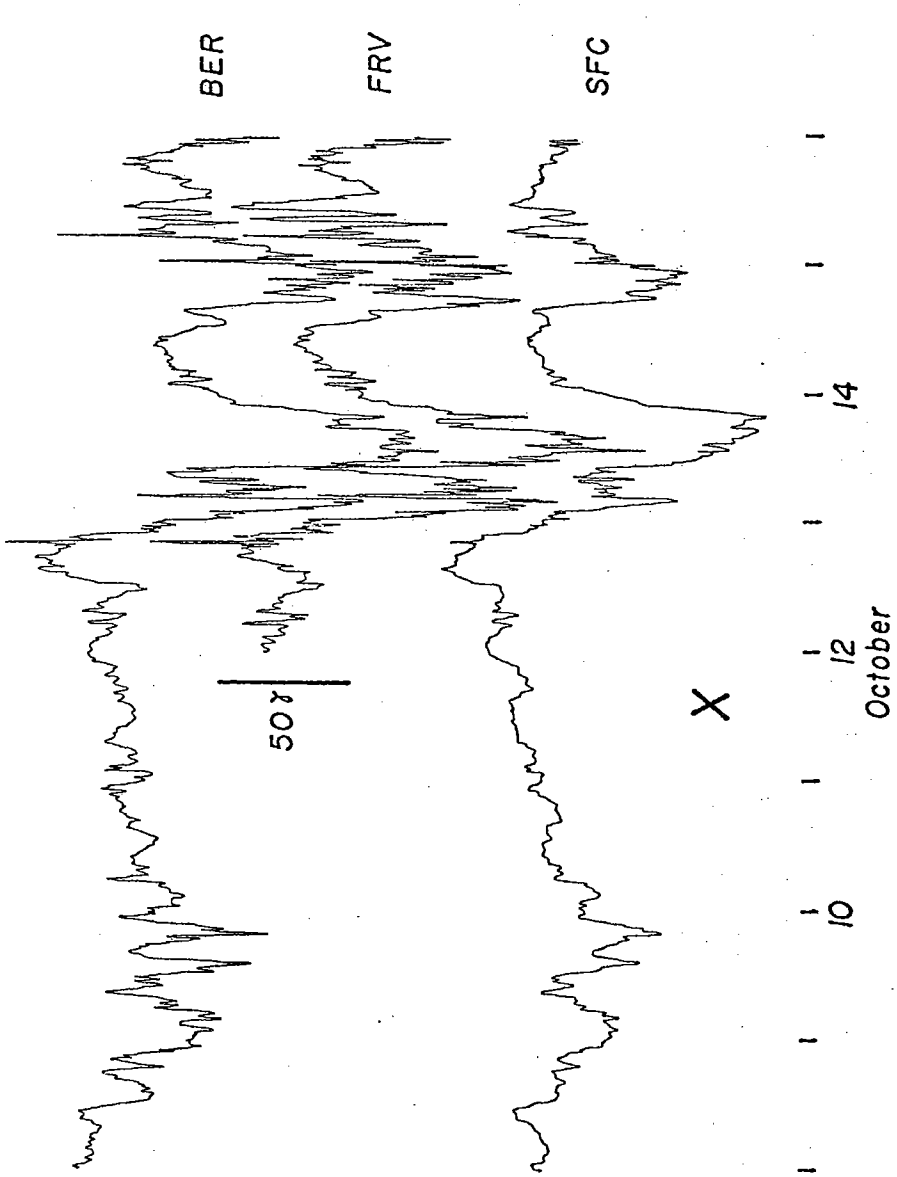

Figure 3.9 Storm and substorm magnetograms from seafloor and reference stations.

for linearly independent variables deteriorates. The greater stability and the observation that the tensor rotation angle is in fact not zero makes it desirable to use a tensor transfer function wherever possible.

The overall results of the tensor analysis are summarized for each site in Figures 3.10 to 3.12. All tensor elements have been rotated into the principal direction and only the diagonal elements are shown in the figures. Off-diagonal elements are usually at least an order of magnitude smaller. However, a few relevant comments are in order. Transfer functions are expected to be well behaved, smooth functions for frequency in both amplitude and phase. This might be true of the amplitude data but it is not true for the phase data even over the more coherent lower frequencies. The Y data certainly shows more variability than the X data. In some cases not shown, the Y phase data has no legitimate frequency dependence whereas the X data is reasonably well behaved.

The possible two-dimensionality or anisotropy in structure indicated by the tensor transfer functions and the rotation angles may be variously interpreted. If the two-dimensionality is structural in origin there should be induced vertical fields and a constant or slowly varying principal direction between

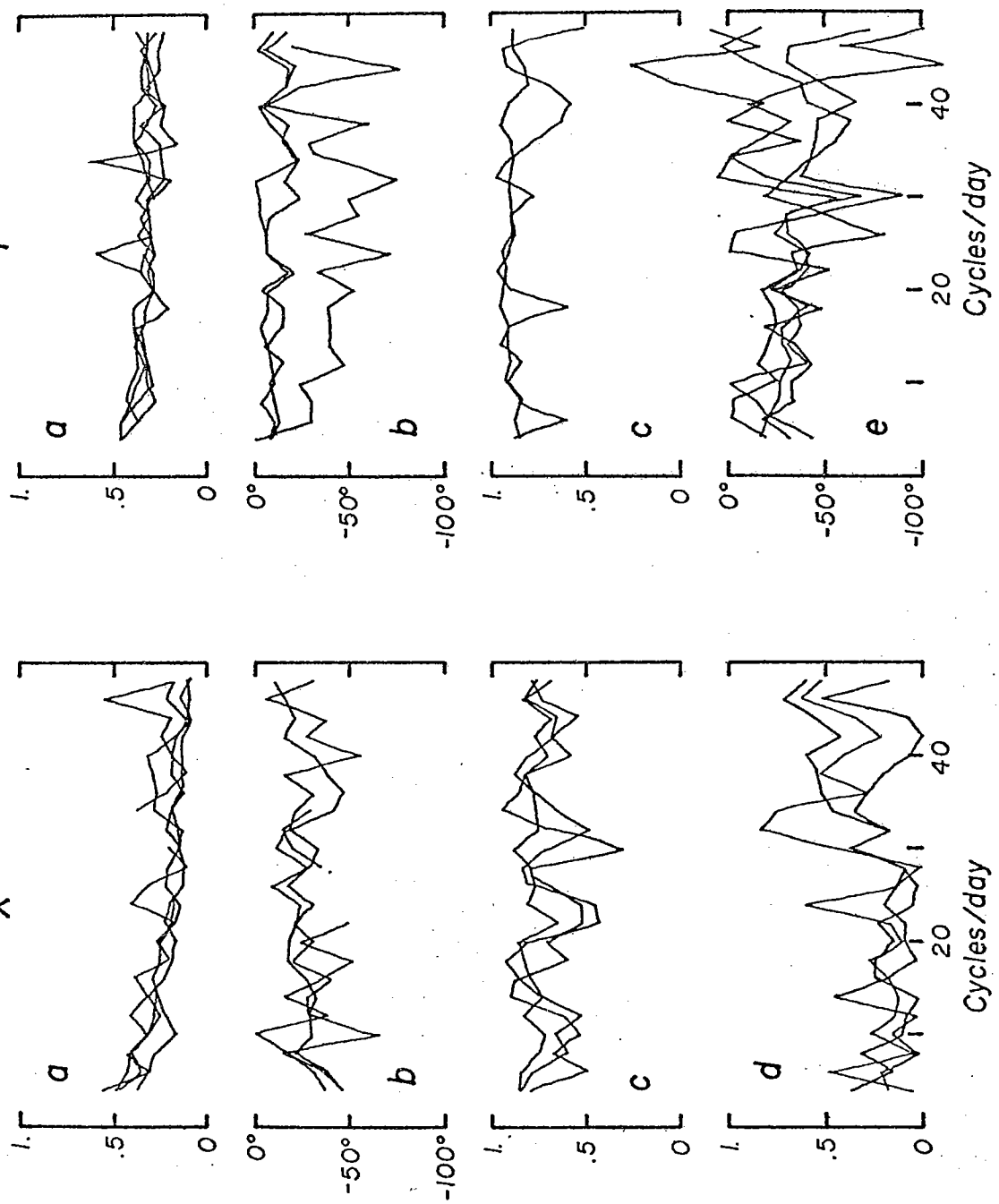

Figure 3.10 Tensor transfer function analyses for SF. a) amplitude of transfer function, b) phase of transfer function, c) multiple coherence between seafloor variations and X_{ref} and Y_{ref}, d) coherence between X and Y at the reference station, and e) principle direction (east of north).

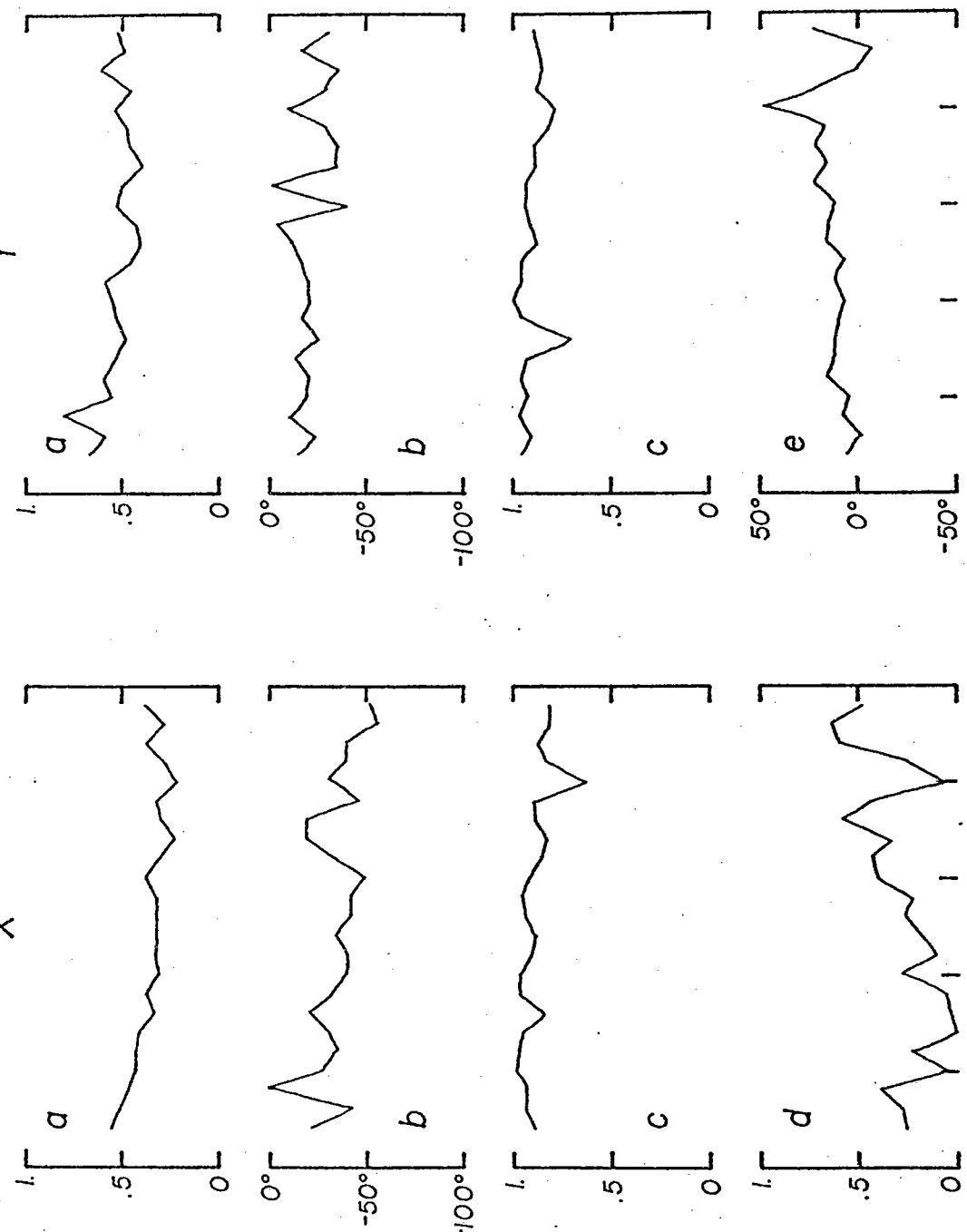

Figure 3.11 Tensor transfer function analyses for SFA. a,b,c,d, and e as in Figure 3.10.

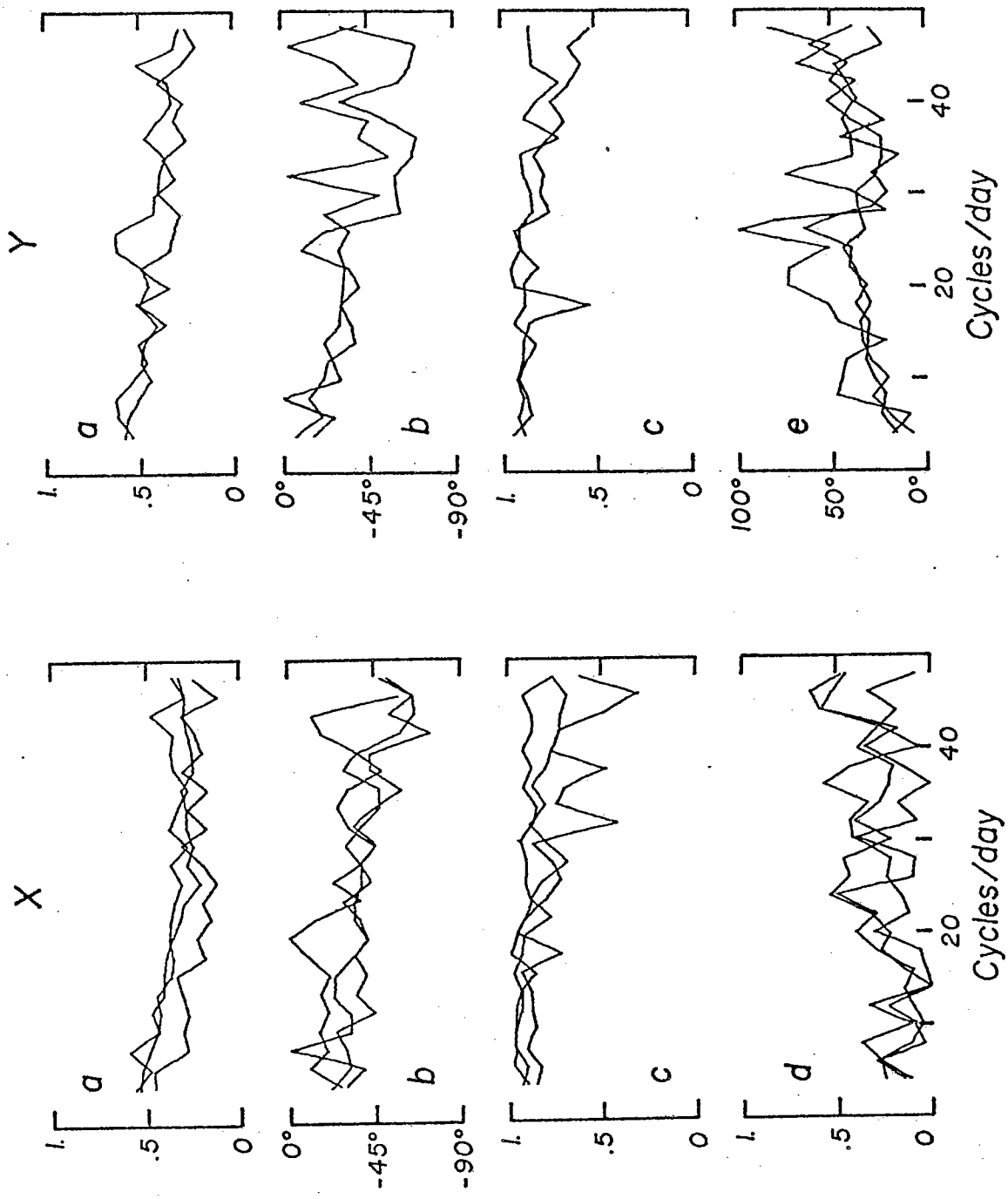

Figure 3.12A Tensor transfer function analyses for SFC. a,b,c,d, and e as in Figure 3.10.

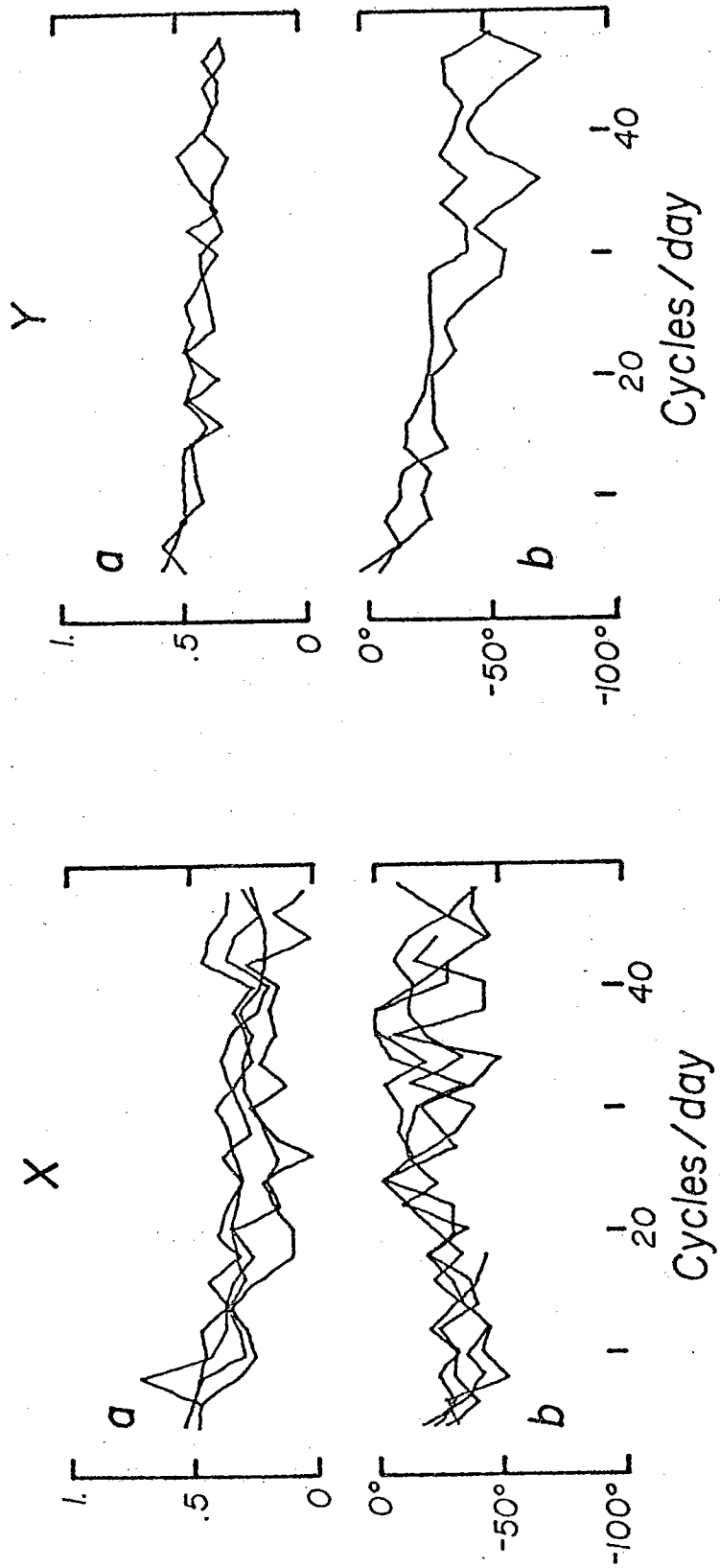

Figure 3.12B Scalar transfer function analyses for SFC. a and b as in Figure 3.10.

vertical and horizontal variations. The vertical field variations on the seafloor are very small in most cases and show no significant coherency (usually less than 0.4) with the horizontal fields. No principal direction could be found. This does not eliminate the possibility of material anisotropy. The conductivity of the lithosphere may be anistropic in a direction similar to tectonic patterns due to preferred orientations of crystals and fabric.

The tensor rotation angle is a poor indicator of structure because it is also dependent upon changing source field configurations. Anomalous horizontal fields are usually much smaller than the inducing field except for cases of extreme inhomogeneities (Porath et al., 1970). Excluding extreme inhomogeneities, the total horizontal variation should be representative of the normal horizontal variation field. No rotation should be observed.

These observations cast significant doubt upon the existence of a two-dimensional seafloor structure. The indicated rotation angle at SFC is close to the strike of the isochrons, but it is also close to the gross strike of the Bermuda Islands. The rotation angle at SF bears little resemblance to any observable geological features; it reflects

the rotation of the fields between FRV and BER. It seems equally likely that the rotation angles are the result of changing source fields and that the poor quality of the Y results somehow reflects their greater spatial variability.

The final transfer functions are calculated by fitting a smooth curve to both the amplitude and phase data. Confidence limits are determined by drawing an envelope enclosing the body of data and dividing the width of the envelope by the square root of the number of events enclosed. This seems to be a reliable measure of the total uncertainty involved in the calculation.

3.5 IN RETROSPECT

As the next chapter will bring out, electromagnetic data inversion utilizes some form or complex impedance of the apparent resistivities. The vertical gradient method of analysis immediately results in the estimation of a complex transfer function which can be related to the impedance. However, only the amplitude of the transfer function has been well determined. As can be seen from equation 1.2, a complex transfer function is required to calculate a complex impedance or even to calculate the amplitude of the impedance (apparent resistivity). The amplitude of the transfer function contains

even less information than the amplitude of the impedance. If a poorly determined transfer function phase is used to calculate the impedance, the phase error spills over into the error in impedance amplitude.

These considerations place grave doubts on the utility of the vertical gradient method for calculating anything but general conductivity structures within the oceans. Unless the seasurface station is close to the seafloor site and free from local disturbances only poor quality data can be expected. This problem, along with the unusable vertical field variations on the seafloor in this study, greatly limit the usefulness of a purely magnetic analysis to anything but first order surveys. Clearly, simultaneous electric field measurements on the seafloor are required if results comparable to those obtained on land are to be realized in the oceans.

CHAPTER IV

DATA COMPATIBLE RESISTIVITY MODELS

4.1 INTERPRETATION OF THE DATA: PROBLEMS AND LIMITATIONS

The data analysis in Chapter III could be accomplished with a few assumptions and no reference to the model eventually to be used for interpretation. This model must be specified, described and evaluated, however, before any inversion is undertaken. The nature of the data collected limits the interpretation to that of a one-dimensional, layered media with specified source field wavenumber as discussed in Chapter I. With this model as a starting point, impedances or apparent resistivities and phases (Figs. 4.1-4.3) can be calculated from the transfer functions for each site using the vertical gradient of the horizontal fields to estimate the electric field on the seafloor.

Three inconsistencies between data and model become immediately apparent in looking at the apparent resistivity and phase. 1) Apparent resistivities calculated from the tensor impedances decrease at high frequencies much more rapidly than is permitted by the model. Weidelt (1972) has presented four inequalities the data must satisfy for a 1-d model:

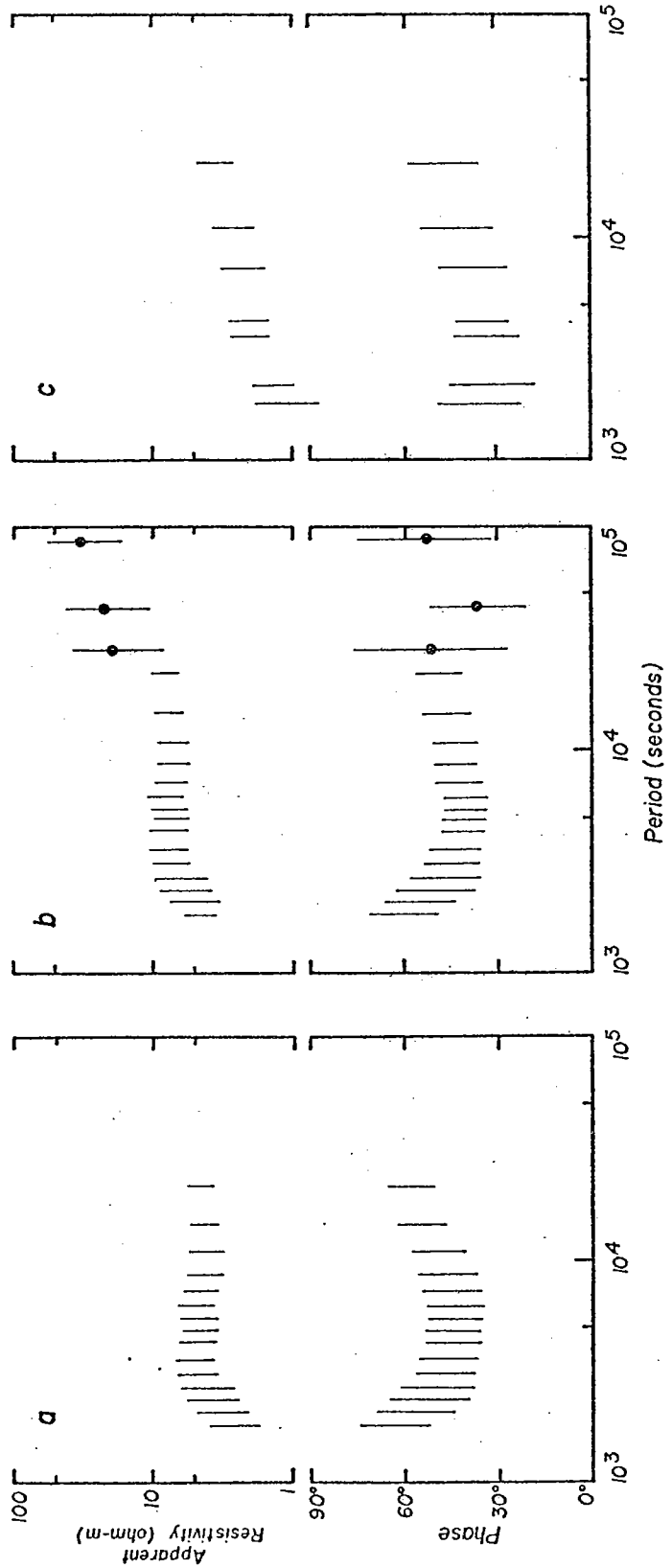

Figure 4.1 Apparent resistivity and phase versus period for SFA. a) latitude corrected for the X component, b) no latitude correction for the X component, and c) no latitude correction for the Y component. Black dots indicate diurnal harmonics.

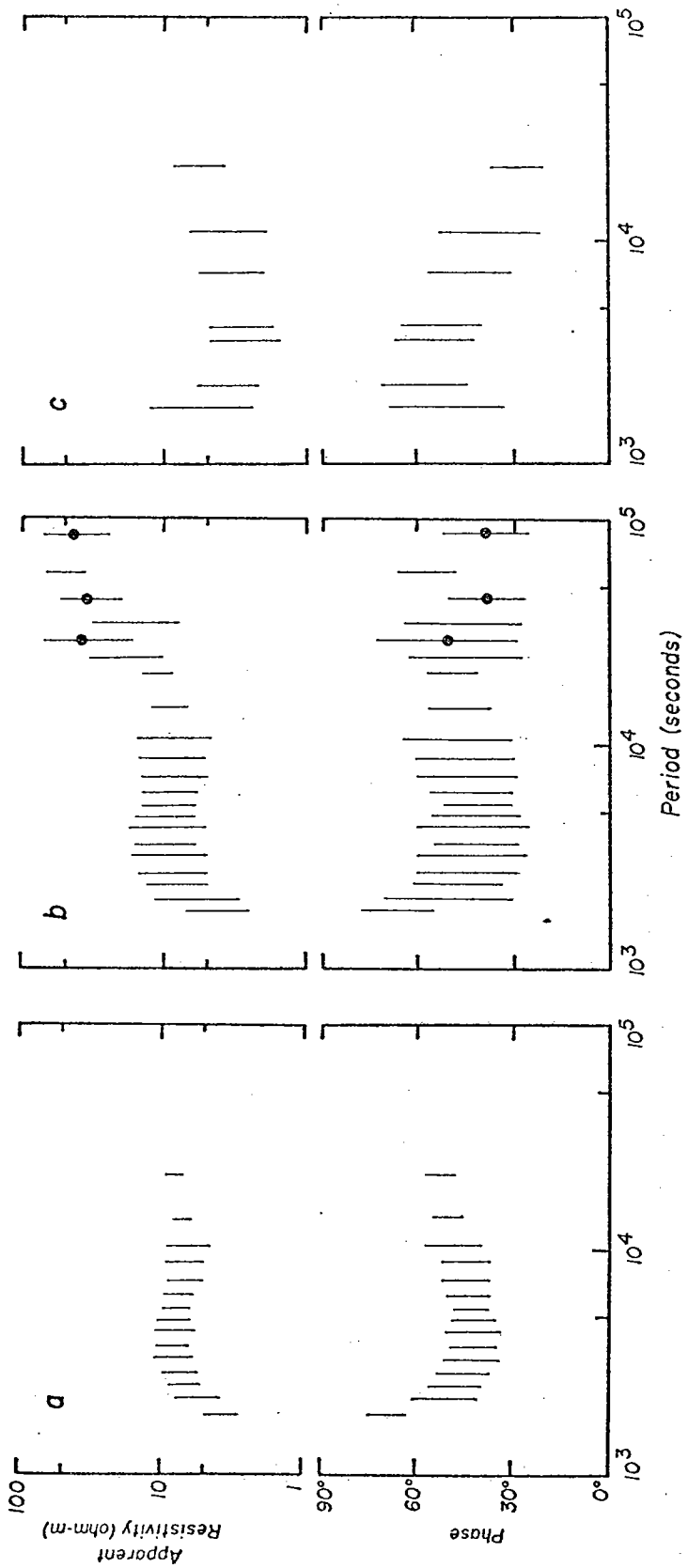

Figure 4.2 Apparent resistivity and phase versus period for SFC. a,b,and c as in Figure 4.1.

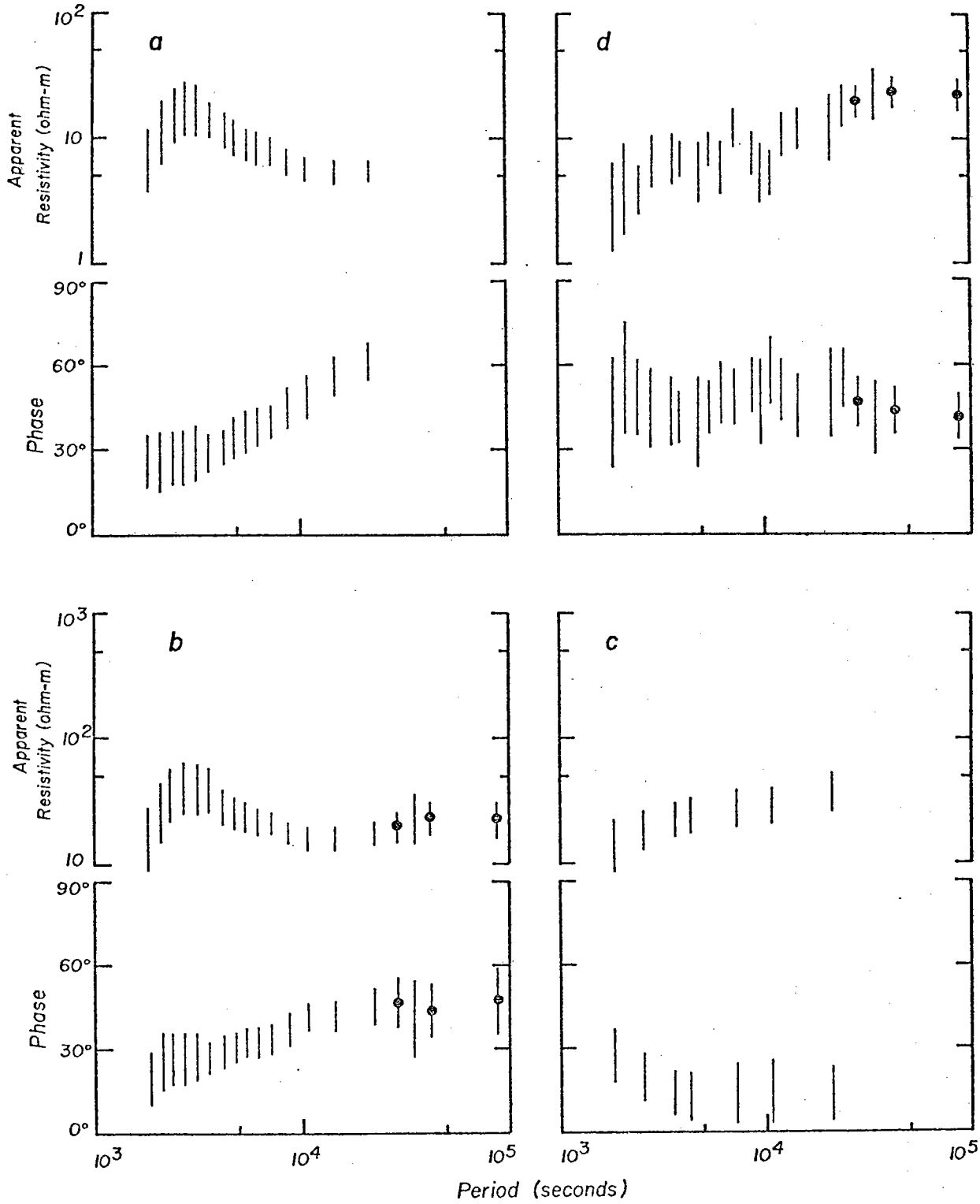

Figure 4.3 Apparent resistivity and phase versus period for SF. a,b, and c as in Figure 4.1. d) from scalar transfer functions.

$$0 \leq \psi \leq \pi/2$$

$$-\rho_a \leq D\rho_a \leq \rho_a$$

$$\tfrac{1}{4}(1 - D\rho_a/\rho_a)^2 + (D\psi)^2 \leq \sin^2\psi$$

$$\tfrac{1}{4}(1 + D\rho_a/\rho_a)^2 + (D\psi)^2 \leq \cos^2\psi$$

where ψ is the phase of the impedance, ρ_a is the apparent resistivity and D is the operator $-\frac{d}{d\log T}$. This rapid decrease is not as pronounced in the scalar resistivities. 2) In all cases apparent resistivities calculated from the diurnal harmonics do not merge with those from the continuum analysis. Long period (greater than 6 hours) continuum resistivities calculated using high resolution cross-spectra fall between those for the diurnal and continuum analysis. 3) Tensor resistivities at SF do not approximate the non-tensor resistivities as is the case at the other stations.

In order to explain the origins of these inconsistencies it is advantageous to review the stages of data processing with the expressed purpose of determining how each step affects the impedance approximated by equation 1.3 $\left(Z(\omega) = \frac{R-1}{\sigma_{1,d}}\right)$. In the following we will define $Z_{sf} = a + ib$ and $R = r(\cos\phi + i\sin\phi) = s + it$. So we have $a \propto r\cos\phi - 1$ and $b \propto r\sin\phi$. Changing the phase ϕ effects a and b oppositely while changing the amplitude r effects them in the same sense. Apparent resistivity is proportional to $r^2 - 2r\cos\phi + 1$ and is thus

more dependent upon r than upon $\emptyset$; a 20% error in $\emptyset$ only results in about a 5% error in apparent resistivity in many cases (if $\emptyset$ is much greater than 45° the error will be larger).

Calibration errors have already been discussed in Chapter II and are unlikely to significantly contribute to the preceding problems. However, the timing errors discussed may contribute to the first problem. The error in phase ($\Delta \emptyset$) caused by a timing error (Δ t) is $\Delta t \times 360°/T$, where T is the period. Sampling intervals for all data range from 64 to 150 seconds; errors of this magnitude might be expected. The timing problems noted at BER could have resulted in larger errors, but all data sections were visually realligned to correct for any cumulative errors. The timing reallignment should eliminate errors longer than the sampling interval. A short calculation reveals that a 100 second timing error with BER ahead of SFC brings the SFC data into accord with Weidelt's four criteria; a 45 second error is calculated at SFA. A timing error cannot account for the high frequency problem at SF because of the low magnitude of b. It should be remembered that an underestimate of r at high frequencies is an alternative explanation.

Other amplitude and phase errors may be introduced through poor estimates of the transfer function (A) between the sea-floor (sf) and sea surface (ss). In the most general case we want to solve the matrix equation $H^t_{sf} = (A)\ H^t_{ss}$ where the superscript "t" denotes the total field, and "n" the normal field. Since it is impossible to estimate anomalous fields at the sea surface (hence the assumption of one-dimensionality), it must be assumed that $H^t_{ss} = H^n_{ss}$, that H^n_{ss} can be calculated from H^n_{ref} ($H^n_{ss} = (C)\ H^n_{ref}$), and that H^n_{ref} can be calculated from H^t_{ref} ($H^n_{ref} = (B)H^t_{ref}$). A more representative equation is seen to be $H^t_{sf} = (A)(C)(B)H^t_{ref}$. It now becomes evident that knowledge of the reference station structure (B) and the spatial variations of the normal fields (C) is more than of just passing concern.

Both FRV and BER may be anomalous due to their location: FRV a coastal station and BER an island station. FRV is observed to have an anomalously low coast effect (Hyndman and Cochrane, 1971) probably due to high conductivity well inland (Edwards and Greenhouse, 1975). The coast effect is usually seen in anomalous vertical magnetic fields with only small anomalous horizontal fields (Schmucker, 1970). These small anomalous horizontal fields should not significantly affect

the usefulness of FRV as a reference station. The anomalous horizontal fields associated with other local structures at FRV are also believed to be negligible (Greenhouse, personal communication). Islands are known to have negligible anomalous horizontal fiels over most of the interior, especially if there is little vertical field activity (Larsen, 1968; 1975). No information is presently available detailing the magnetic response of Bermuda, so both conditions are assumed to be satisfied. Present knowledge therefore indicates that (B) can be considered unity at both reference stations.

The estimation of (C), the transfer function for the normal field variation, is extremely difficult utilizing only three land stations. The wavenumber calculated in Chapter III was taken as being frequency independent and equivalent for X and Y fields. Both of these assumptions become suspect upon closer scrutiny. The wavenumber was calculated from 5 day active record sections and thus averages many events. If shorter record segments are chosen it is found (not unexpectedly) that the wavenumber shows considerable temporal variation. However, since it is neither practical nor convenient to calculate a separate wavenumber for individual events, this study assumes no temporal variation. The possibility of

frequency dependence is real, as well as a different wavenumber for X and Y components. A smaller wavenumber for long periods and for the Y component is suggested by the ratios in Table 3.1. Apparent resistivities calculated from continuum data with no latitude correction (k=0) are in better accord with the diurnal data.

Also included in (C) is the difference in inductive response between land and ocean, and magnetic fields induced by water motion. The latter contribution cannot be predicted. Little is known about the spectrum of motion induced currents within the deep oceans. Contributions at tidal frequencies are known to be significant (Larsen, 1968), but induced magnetic fields due to internal waves and currents are probably small (Cox et al., 1970). The calculated electric field will differ from the measured field because contributions due to the motion of seawater must be ignored at the seasurface. The higher conductivities beneath the ocean might result in larger horizontal fields over the ocean than over the land. Bermuda is an island station and subject to the oceanic conductivity structure, so horizontal field enhancement between BER and SF should be negligible. It is not clear how the structure at FRV affects the field amplitudes. FRV is a

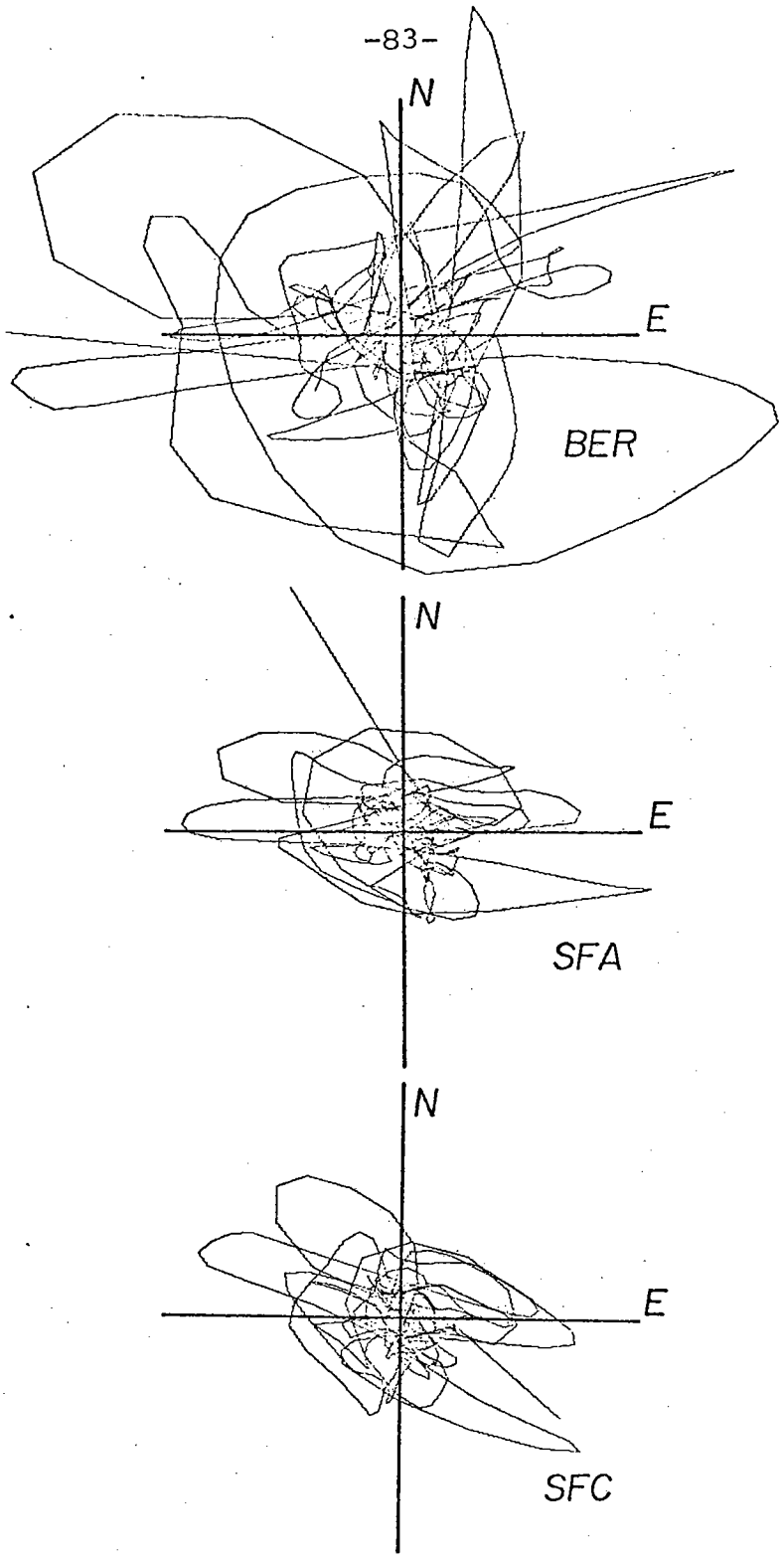

Figure 4.4 Hodograms for first day of AA#8 at three stations. Axes are 25 gammas in length. Change in shape or orientation of major features is indicative of spatial changes in source field configuration or morphology.

coastal station with a relatively high near surface conductivity. The horizontal field amplitudes are usually doubled at the surface of any conductor (Price, 1950)(except when the source field wavelength becomes comparable or smaller than the skin depth) so that the response of the reference station to horizontal variations can be taken as equal to that of the oceans.

The brief discussion of tensor rotation angles in Chapter III intimated an origin related to source field variations. In review, it was argued that the usually small anomalous horizontal fields (if any exist) cannot cause substantial total field rotation. The absence of induced vertical fields on the seafloor further argues against a two-dimensional structure. A comparison of the magnetograms for seafloor and reference stations (Figs. 3.8 and 3.9) clearly shows a variation in the shape of the substorms recorded at the different sites. Hodograms (Fig. 4.4) plotted for different substorms further confirm the changing field conditions. The tensor rotation angles do suggest that the field change is largely in the form of a simple rotation that will not affect the results.

The wavenumber appears in the analysis in two ways: 1) as a correction in amplitude for latitude and longitude (which unfortunately cannot be separated in this case) and

2) as a structurally related parameter in the impedance function. The difference between no latitude correction and the calculated correction upon the apparent resistivities and phase is illustrated in Figures 4.1 and 4.3. The values obtained for no correction merge well with the diurnal estimates (referenced to BER). The change is of course less dramatic at SFA and SFC where the correction is much smaller. The Y transfer functions might become more useful with a better latitude/longitude correction, although the correction would not substantially improve the poor phase estimates. A frequency dependent correction would provide almost endless variations on the results but cannot be discredited.

It is well known that short source field wavelengths affect the calculated impedances (Price, 1962; Srivastava, 1965). Basically, what is seen is a decrease in apparent resistivity and an increase in phase as the wavelength decreases. This same effect is observed by over-correcting for latitude/longitude. Another look at the data presented in Figures 4.1 and 4.3 shows that this trend may exist and might explain the discrepancy between continuum and diurnal results. However, the wavelength required to produce the observed trends is approximately 1000-2000 km, much shorter than that calculated here (10000-20000 km) and shorter than that

observed on land (5000-10000 km)(Porath et al., 1971). Our measurements, however, cannot completely discredit such a short wavelength, but the explanation centered around the latitude correction seems more likely.

Before discussing the possible models consistent with the data it is informative to qualitatively compare the electric field predicted by the vertical gradient method with that actually measured at the seafloor (Fig. 4.5). Plots of the seafloor electric field measurements become available only at the latter stages of this study. However, several of the questions brought out in the last section can be partially resolved by this comparison.

The vertical gradient method essentially calculates the difference between the seafloor and reference station magnetograms; the much larger short period activity at FRV will dominate the electric field. A close inspection of the magnetograms also shows that the changing magnetic field morphology carries over strongly into the electric field, especially at the longer periods. The apparent differences between the calculated and observed electric field probably result from the changing source field morphology.

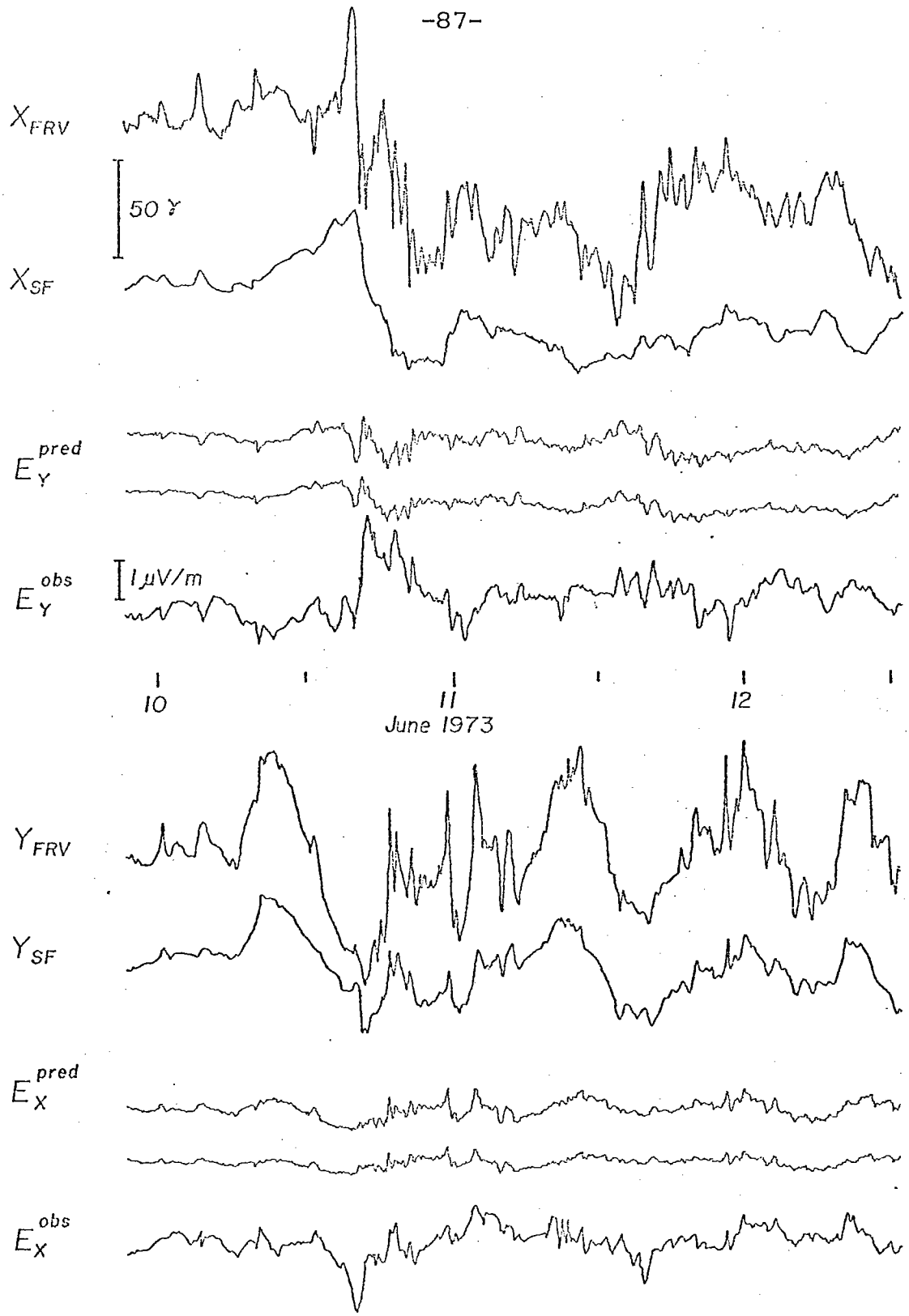

Figure 4.5 Magnetic fields recorded at FRV and SF compared to predicted and observed electric fields on the seafloor. Upper predicted E field is with no latitude correction and the lower with a 30% reduction in amplitude for the FRV variations.

A reasonably good evaluation of our latitude/longitude corrections can be made by comparing the calculated and observed amplitude of events. The X component latitude correction (multiplication factor of 0.7 to amplitude of FRV variations) is good for the high frequency (greater than 12 cpd) events but should be less drastic (about 0.9-0.95) for increasingly lower frequencies. It appears that on the average no latitude correction (1.0) is required for the Y component. The diurnal harmonics may be overestimated in both components, although it is not known how much of this difference can be attributed to tidal influences.

The true and only real test of how well the electric field is predicted must await a spectral analysis of the observed and predicted fields. Even if thetwo appear to be different, their band-averaged spectral estimates or at least their power spectra may be comparable.

The search for conductivity models compatible with the observations will now be undertaken from several points of view. The uncertainties in the data discussed in the previous section will be appreciated by considering models that independently match one of two data sets. The first set of data to be modeled will be the latitude/longitude corrected

continuum impedances. The second set of data will consist of the uncorrected continuum data plus the diurnal harmonics and low frequency data where available. In all cases, except for the use of scalar data where X and Y components have been averaged, only impedances obtained from the X component will be matched. The X impedances are judged to be of better quality than the Y impedances. This should cause no loss of model generality since the conductivity structure is believed to be one-dimensional.

4.2 APPARENT RESISTIVITY AND PHASE

Before proceeding to more formal modeling it is instructive to gain some insight into the expected models and problem areas through a qualitative evaluation of the apparent resistivity and phase. The SFA and SFC results are quite similar and will be discussed together followed by a discussion of the SF results.

Similar trends can be identified both in the apparent resistivity and phase at SFA and SFC (Figs. 4.1 and 4.2). Apparent resistivities of the continuum remain fairly constant except for a rapid decrease at short periods. Resistivities at SFA average about 4-5 ohm-m (8 ohm-m uncorrected) while those at SFC are slightly higher at 8 ohm-m (9-10 ohm-m uncorrected). Phases at both sites exhibit minima around

4000 seconds but the phases of uncorrected data are lower and less variable. There is an increase in phase coinciding with the decrease in resistivity. This, of course, is exactly opposite to physical expectations and probably results from the previously discussed timing errors. In the following modeling no attempt will be made to match these data. It should be noted however, that the resistivity and phase still show the same trends but to less degree after the timing correction is made indicating there still may be another problem with the high frequency data or the timing correction may be larger than anticipated.

The diurnal harmonics indicate resistivities still increasing at greater depths. The larger error bars for the diurnal results only overlap those for the uncorrected continua on the high resistivity extreme. The diurnal phases predict a constant or increasing resistivity at depth.

To summarize, the apparent resistivities at both sites appear to increase from about 5-10 ohm-m near the surface to more than 20 ohm-m at greater depths. The phases, however, suggest constant or low resistivity near the surface, a layer of maximum resistivity, and decreasing resistivity below. The diurnal results tend to give a lower bound to deep resistivities of about 15-30 ohm-m. Skin depth estimates for the above

resistivities imply that the period range at hand can best resolve structures within the depth range 50-150 km. There will be little resolution of the shallow structure which possibly contains the near surface low resistivity.

Data curves for SF (Fig. 4.3) are significantly different from those described above. The apparent resistivity shows a strong maximum at 3000 seconds. The low resistivity values on both sides of the maximum are not compatible with Weidelt's four constraints; the contrast in apparent resistivity must be smaller. However, the trend in the phase curve is consistent with such a structure. There is a much greater disparity between corrected and uncorrected data at this site because it is referenced to FRV instead of to BER. The true resistivity curve possibly is some amalgamation of the two curves and the diurnal estimates. The amalgamation may be represented by the scalar results in Figure 4.1d. If this is the case, the structure at SF may be similar to the other sites but with higher resistivities. (Later model studies will show that this may well be the case.) If higher resistivities are found at SF, the structure will be even more poorly resolved near the surface but will be resolved to greater depths.

As a final word, it should be remembered that apparent resistivity is an integrative measure of the true resistivity. The true resistivity may have different trends that are only illuminated by the phase data. Resistivity is generally expected to decrease at depth due to increasing temperatures. Even though the apparent resistivities increase with depth the actual model may show decreasing resistivites starting at some depth below the surface; the apparent increase with depth may be caused by a low resistivity surface layer which dominates the structure.

4.3 MONTE CARLO MODELING

The formal search for suitable resistivity models is carried out using a one-dimensional Monte Carlo inversion program provided by Dr. John Hermance. Models calculated from the Monte Carlo program agree with those calculated by other means. Basically, the technique is simply a high-speed algorithm for calculating and evaluating models within pre-designated bounds. The program is supplied with a layered structure with upper and lower limits on the resistivity within each layer. Starting with the lowest frequency the program calculates the apparent resistivity and phase and compares them to the observations. If the model is compatible

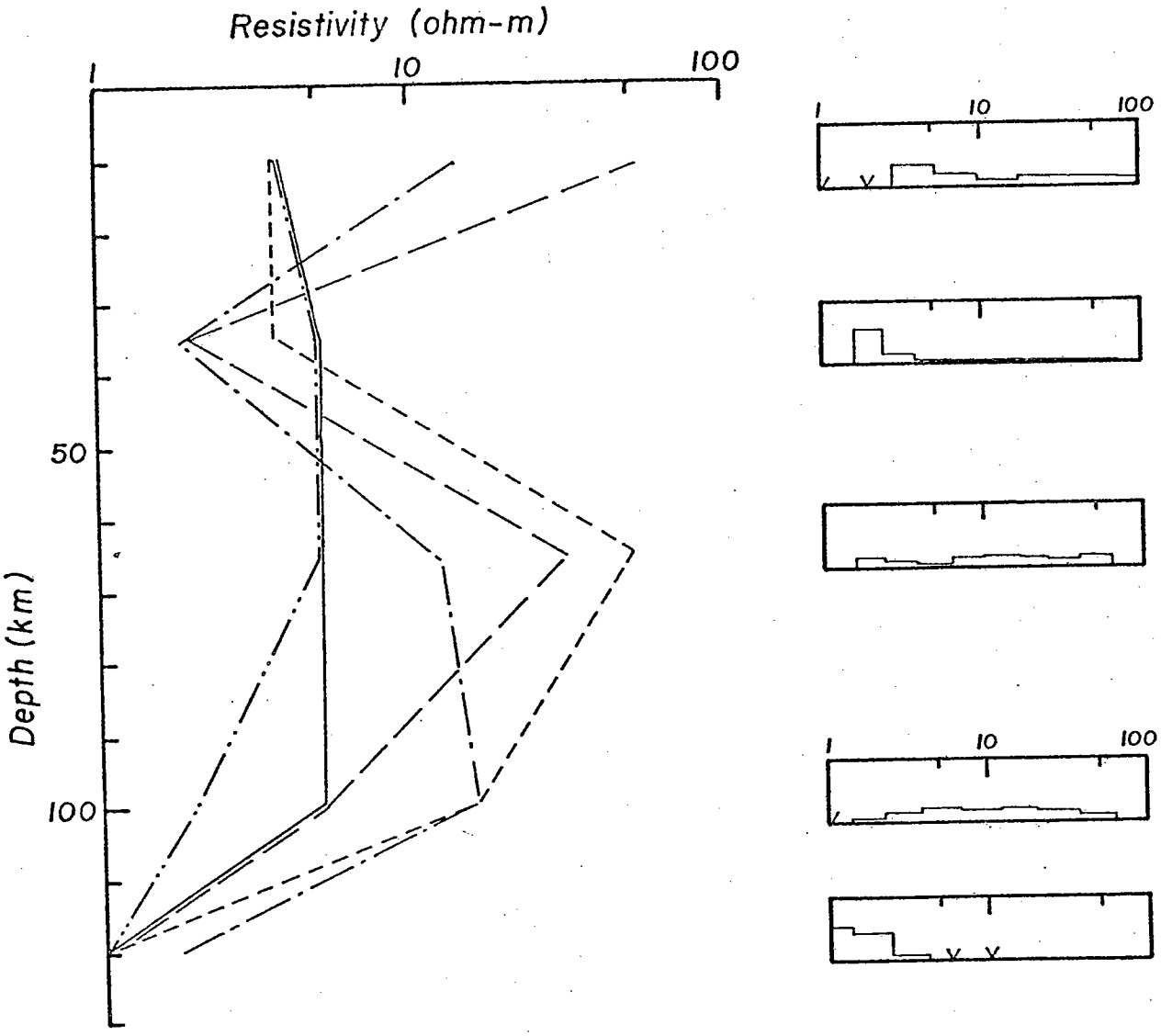

Figure 4.6a SFA Monte Carlo models fitting latitude corrected continuum data. Vertical axis on histogram boxes is 100%. V's indicate resistivities included in the search but with null results.

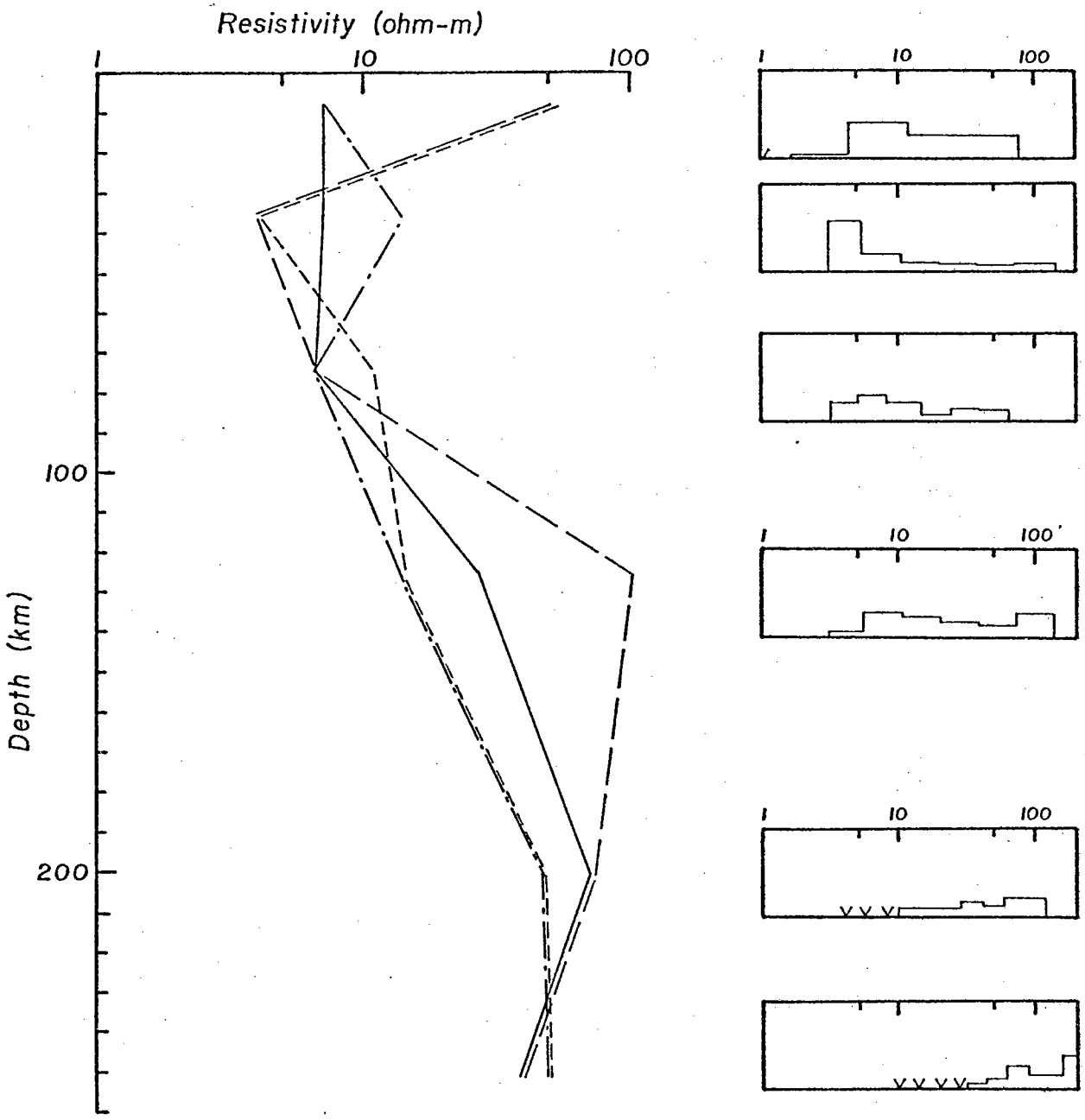

Figure 4.6b SFA Monte Carlo models fitting continuum data with no latitude correction and the diurnal harmonics.

at that frequency the apparent resistivity and phase are calculated and compared at another frequency. As soon as a mismatch is found the model is rejected, thus saving time. Models are chosen for comparison within the prescribed limits by a pseudo-random number generator. Approximately one-half of the potential models are evaluated in a complete computer run.

Monte Carlo models are only constrained by the prescribed layering and resistivity bounds. Since the layering (number and thickness) is specified, it must be known a priori if the correct resistivity distribution is to be found. The method is not designed to easily study a variety of layer thicknesses. However, the details of the layering are only useful if they are well resolved. (The resolution of the data will be discussed later in terms of the structures found.) The results of the Monte Carlo study will be presented in the form of several representative structures and as the distribution of resistivity occurrences within each layer.

The models found to fit SFA and SFC (Figs. 4.6a and b, and 4.7a and b) are similar and will be discussed together. The distributions show that the structures might be simply interpreted as a higher resistivity layer sandwiched between two

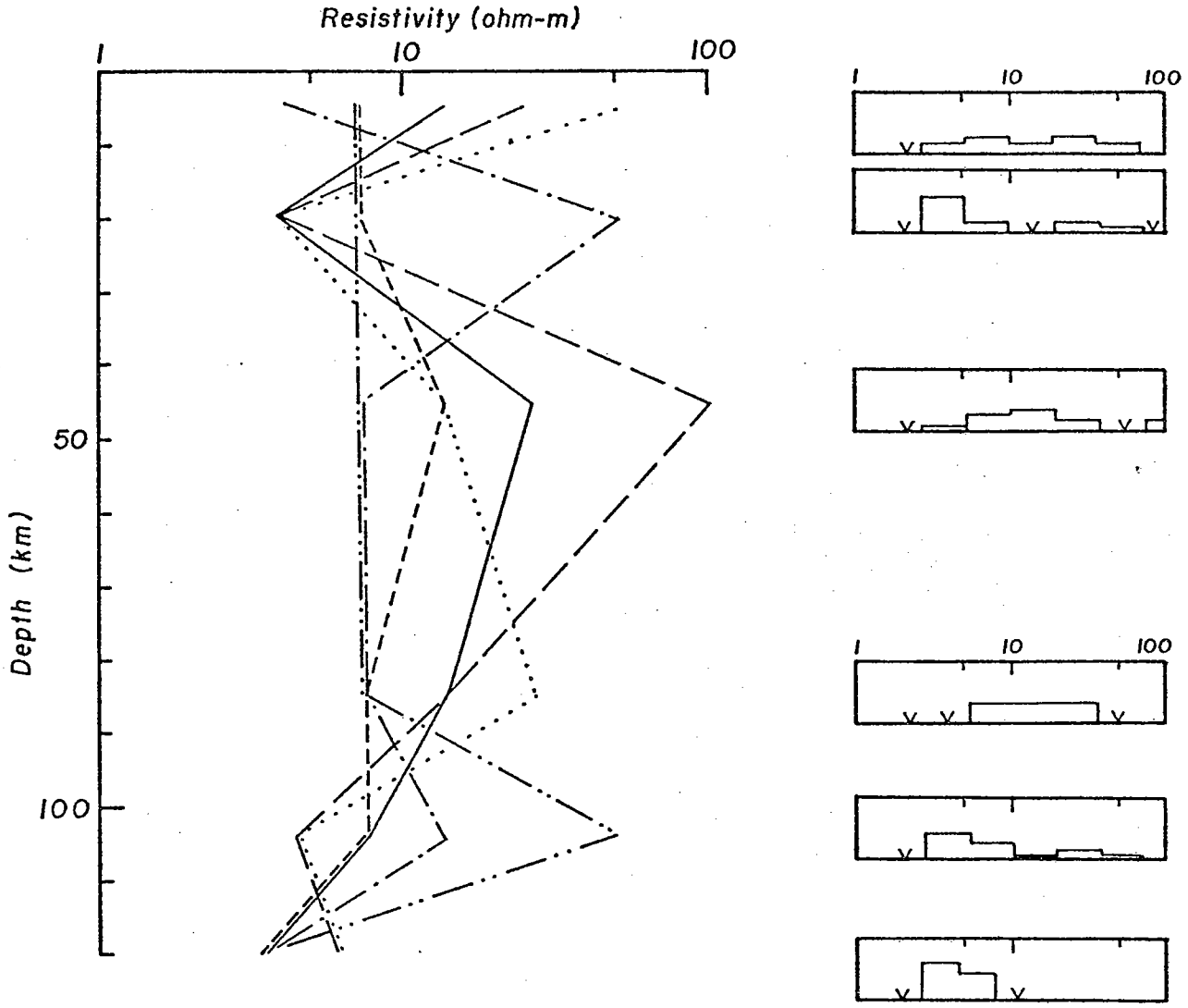

Figure 4.7a SFC Monte Carlo models fitting the latitude corrected continuum data.